remote sensing

MDPI

Article

Quantitative Assessment and Impact Analysis of Land Surface Deformation in Wuxi Based on PS-InSAR and GARCH Model

Shengyi Zhang [1], Lichang Xu [1], Rujian Long [1], Le Chen [1], Shenghan Wang [1], Shaowei Ning [1,*], Fan Song [2,3] and Linlin Zhang [1]

[1] College of Civil Engineering, Hefei University of Technology, Hefei 230009, China; blackjack@mail.hfut.edu.cn (S.Z.); lichangxu@mail.hfut.edu.cn (L.X.); rujian524@mail.hfut.edu.cn (R.L.); 2021216283@mail.hfut.edu.cn (L.C.); wangshenghan@mail.hfut.edu.cn (S.W.); linlinzhang@hfut.edu.cn (L.Z.)
[2] Information Center (Hydrology and Water Resources Monitoring and Forecasting Center), The Ministry of Water Resources of China, Beijing 100038, China; songfan1989@mwr.gov.cn
[3] Hydrology and Water Resources Monitoring and Evaluation Center (National Groundwater Monitoring Center), The Ministry of Water Resources of China, Beijing 100053, China
* Correspondence: ning@hfut.edu.cn

Abstract: Land surface deformation, including subsidence and uplift, has significant impacts on human life and the natural environment. In recent years, the city of Wuxi, China has experienced large-scale surface deformation following the implementation of a groundwater abstraction ban policy in 2005. To accurately measure the regional impacts and understand the underlying mechanisms, we investigated the spatiotemporal characteristics of surface deformation in Wuxi from 2015 to 2023 using 100 Sentinel-1A SAR images and the Persistent Scatterer InSAR (PS-InSAR) technique. The results revealed that surface deformation in Wuxi exhibited significant spatial and temporal variations, with some areas experiencing alternating trends of subsidence and uplift rather than consistent unidirectional change. To uncover the factors influencing this volatility, we conducted a comprehensive analysis focusing on groundwater, precipitation, and soil geology. This study found strong correlations between the groundwater level changes and surface deformation, with the soft soil geology of the area, characterized by alternating layers of sand and clay, further increasing the surface volatility. Moreover, we innovatively applied the Generalized Autoregressive Conditional Heteroskedasticity (GARCH) model, typically used in financial analyses, to analyze the subsidence displacement time series in Wuxi. Based on this model, we propose a new "Amplitude Factor" index to evaluate overall surface deformation volatility in the city. Our qualitative assessment of surface stability based on the Amplitude Factor was consistent with research findings, demonstrating the accuracy and effectiveness of the proposed model. These results provide valuable insights for urban planning, construction, and safety control, highlighting the importance of continuous monitoring and analysis of surface deformation volatility for the city's future development and safety.

Keywords: surface deformation volatility; PS-InSAR; GARCH model; Sentinel-1A; Wuxi city

check for updates

Citation: Zhang, S.; Xu, L.; Long, R.; Chen, L.; Wang, S.; Ning, S.; Song, F.; Zhang, L. Quantitative Assessment and Impact Analysis of Land Surface Deformation in Wuxi Based on PS-InSAR and GARCH Model. *Remote Sens.* **2024**, *16*, 1568. https://doi.org/10.3390/rs16091568

Academic Editor: Giuseppe Casula

Received: 21 March 2024
Revised: 18 April 2024
Accepted: 22 April 2024
Published: 28 April 2024

Copyright: © 2024 by the authors. Licensee MDPI, Basel, Switzerland. This article is an open access article distributed under the terms and conditions of the Creative Commons Attribution (CC BY) license (https://creativecommons.org/licenses/by/4.0/).

1. Introduction

Land surface deformation refers to changing trends in surface morphology within a certain spatiotemporal range, including subsidence, uplift, and horizontal motion. Both subsidence and uplift significantly impact human life and the natural environment [1–3]. Land subsidence is a geological phenomenon where the Earth's surface continuously decreases over time due to anthropogenic or natural factors [4]. Conversely, land uplift refers to the Earth's surface curving upward in a region due to factors such as crustal movement or groundwater level changes [5]. Regardless of whether it is subsidence or uplift that occurs, both reduce the surface stability and trigger geological hazards [6–8]. Moreover, if an area experiences both subsidence and uplift simultaneously, buildings and underground

pipeline networks will suffer severe damage, causing immeasurable losses to human society. For example, Shi et al. monitored Xi'an, China from 2007 to 2019 and found that land surface deformation from rapid urbanization severely impacted subway construction and buildings [9]; Svigkas Nikos et al. studied land surface deformation in Kalochori and Sindos, northern Greece and found that significant subsidence then partial uplift had occurred over the past 55 years, largely related to human activities and deserving managerial attention [10]. Per the United Nations Hydrological Organization predictions, by 2040, land surface deformation will affect over 1.6 billion people worldwide [11]. Therefore, dynamic high-precision monitoring of surface elevation is indispensable.

Traditional monitoring methods for land surface deformation include geodetic surveying and GNSS measurement techniques [12,13]. However, due to the low spatial density of GNSS method observations, this has impacted the investigation and detection of subsidence funnels. Although traditional geodetic surveying techniques have high accuracy [14], they have high labor costs and limited measurement ranges, with obvious disadvantages [15,16]. In the late 1990s, based on Synthetic Aperture Radar (SAR) technology, a new type of space-to-ground observation technology was developed—Interferometric Synthetic Aperture Radar (InSAR) [17]. However, InSAR technology has specific requirements for interference conditions and is affected by error sources such as instrumental noise, orbital errors, and atmospheric delays, which limit its observation accuracy. At the beginning of the 21st century, based on InSAR technology, time-series InSAR (TS-InSAR) technology was further developed [18]. This mainly has two types: one is represented by Persistent Scatterer InSAR (PS-InSAR), which identifies Persistent Scatterers with high reflection intensity and good coherence in SAR images, and uses related techniques to calculate the deformation of scatterers to obtain land surface deformation information in a studied area; the other is the multi-master image time-series InSAR technology (SBAS-InSAR), represented by the Small Baseline Subset InSAR. In addition, there are some techniques derived from the above two methods, such as the Coherent Target (CT) method and the Interferometric Point Target Analysis (IPTA) method [19]. In recent years, TS-InSAR technology has been widely applied. For example, Zhou et al. used SBAS-InSAR technology to analyze the spatiotemporal changes in land subsidence in Wuhan from 2017 to 2021, and they found that the land subsidence in Wuhan was uneven and mainly concentrated in some specific areas [20]. Meer Muhammad Sajjad et al. used PS-InSAR technology to assess the impact of groundwater depletion and aquifer degradation on land subsidence in Lahore, Pakistan, and on this basis proposed a theory of sustainable urban development [21].

Wuxi City, located in the Su-Xi-Chang subsidence zone and the Yangtze River Delta alluvial plain [22], has experienced large-scale land surface deformation in recent years following the implementation of a groundwater abstraction ban policy in 2005 [23]. To accurately measure the regional impacts, this study innovatively applies the Generalized Autoregressive Conditional Heteroskedasticity (GARCH) model for the first time to analyze the volatility of the land surface deformation in Wuxi. Proposed by Bollerslev, GARCH assesses the volatility of random variables [24]. Compared to previous conditional mean models [25], its advantage lies in not only considering the real-time impacts of random disturbances but also greatly improving the prediction accuracy and efficiency. The GARCH model, also known as the Conditional Heteroskedasticity model, describes the variance of error terms in a statistical model changing under certain conditions, rather than being constant. This implies that data volatility is non-constant but clusters at certain moments, effectively solving volatility clustering in statistics [26]. Moreover, the model adds a GARCH term to the original ARCH model, solving the loss of degrees of freedom that results from having too many parameters and realizing the prediction of time-series data volatility [27]. Affected by groundwater recharge, fluctuations in the surface time-series deformation trend resemble stock prices [28]. Therefore, using GARCH to assess regional volatility is very reasonable and effective.

The literature shows that current research mainly focuses on the Su-Xi-Chang area and Yangtze River Delta, with fewer long-time-series, large-scale investigations of Wuxi [29,30].

To study the recent land surface deformation trends and mechanisms in Wuxi, we processed 100 Sentinel-1A SAR images from November 2015 to June 2023 using PS-InSAR technology. Our analysis stems from multiple perspectives, including groundwater, precipitation, and soil geology. Furthermore, we innovatively applied GARCH to analyze subsidence displacement in Wuxi City and propose a new "Amplitude Factor" index evaluating overall land surface deformation.

2. Study Area and Datasets

2.1. Study Area

Wuxi City is situated in southeastern Jiangsu Province, with geographical coordinates of 31°22′N–32°02′N and 119°59′E–120°38′E. It is a central city in China's Yangtze River Delta economic belt, with a population exceeding 7.46 million. The study area includes the main urban districts of Wuxi City (Xinwu District, Xishan District, Huishan District, Binhu District, and Liangxi District) and Jiangyin City (Figure 1). The study area borders Suzhou to the east, adjoins Taihu Lake to the south, and is adjacent to Zhejiang Province; it borders Changzhou to the west, relies on the Yangtze River to the north, and is separated from Jingjiang City of Taizhou City by the river [31]. The total area of the study area is 2574.71 square kilometers, with plains as the main landform, supplemented by low mountains and remnant hills. The overall topography exhibits a distribution pattern of being high in the southwest and north and low in the central part, with an average elevation of approximately 8 m. Wuxi City belongs to the northern subtropical monsoon climate, located between the Yangtze River and Taihu Lake, with a humid climate and rain in hot seasons. According to the records of the Jiangsu Provincial Bureau of Statistics, the average annual precipitation in Wuxi City is 1142 mm, concentrated in the plum rain season from June to August. There are approximately 5635 rivers within the territory of Wuxi City, with a total area of 939.61 square kilometers, accounting for 20.3% of the city's total area. These rivers, together with the Yangtze River, the Beijing–Hangzhou Grand Canal, and Taihu Lake, form a vast water network [32]. Within the study area, almost all regions are covered by Quaternary loose sediments, mainly composed of silty clay and sub-sand. These two soil layers are interbedded, forming the soft soil geology of the Wuxi area, which has a significant impact on the surface deformation in the region [29,33].

2.2. Datasets

This study utilized 100 Sentinel-1A images provided by the European Space Agency (ESA), spanning from November 2015 to June 2023. These images cover the main urban areas of Wuxi City and Jiangyin City, with absolute differences in acquisition time intervals not exceeding 2 months. The images were acquired using the Interferometric Wide-Swath (IW) mode and VV polarization. Detailed SAR data information is presented in Table 1. Additionally, this study employed the 30 m Shuttle Radar Topography Mission (SRTM) digital elevation model (DEM) from the National Aeronautics and Space Administration (NASA) to remove the topographic phase and the precise orbit data (POD) released by ESA to refine the orbital information, improving the georeference and baseline estimation accuracy.

Table 1. Specific parameters of the Sentinel-1A SAR images.

Parameter	Value	Parameter	Value
Product type	Sentinel-1A	Incidence angle	42.8°
Wavelength	C-band	Path	69
Flight direction	Ascending	Resolution	2.3 m × 13.9 m
Polarization	VV	Number of images	100
Beam mode	IW	Time range	November 2015–June 2023

This study collected various data related to surface changes in the Wuxi area. Groundwater data were obtained from the Jiangsu Bureau of Geological Survey. We selected six evenly distributed monitoring wells and obtained corresponding water level data to

study the relationships between surface deformation and pore-confined water. The China Meteorological Administration provided precipitation data, and the Chinese Academy of Geological Sciences provided geological data. This study utilized geological borehole data to determine the depth of Quaternary sediments in the Wuxi area.

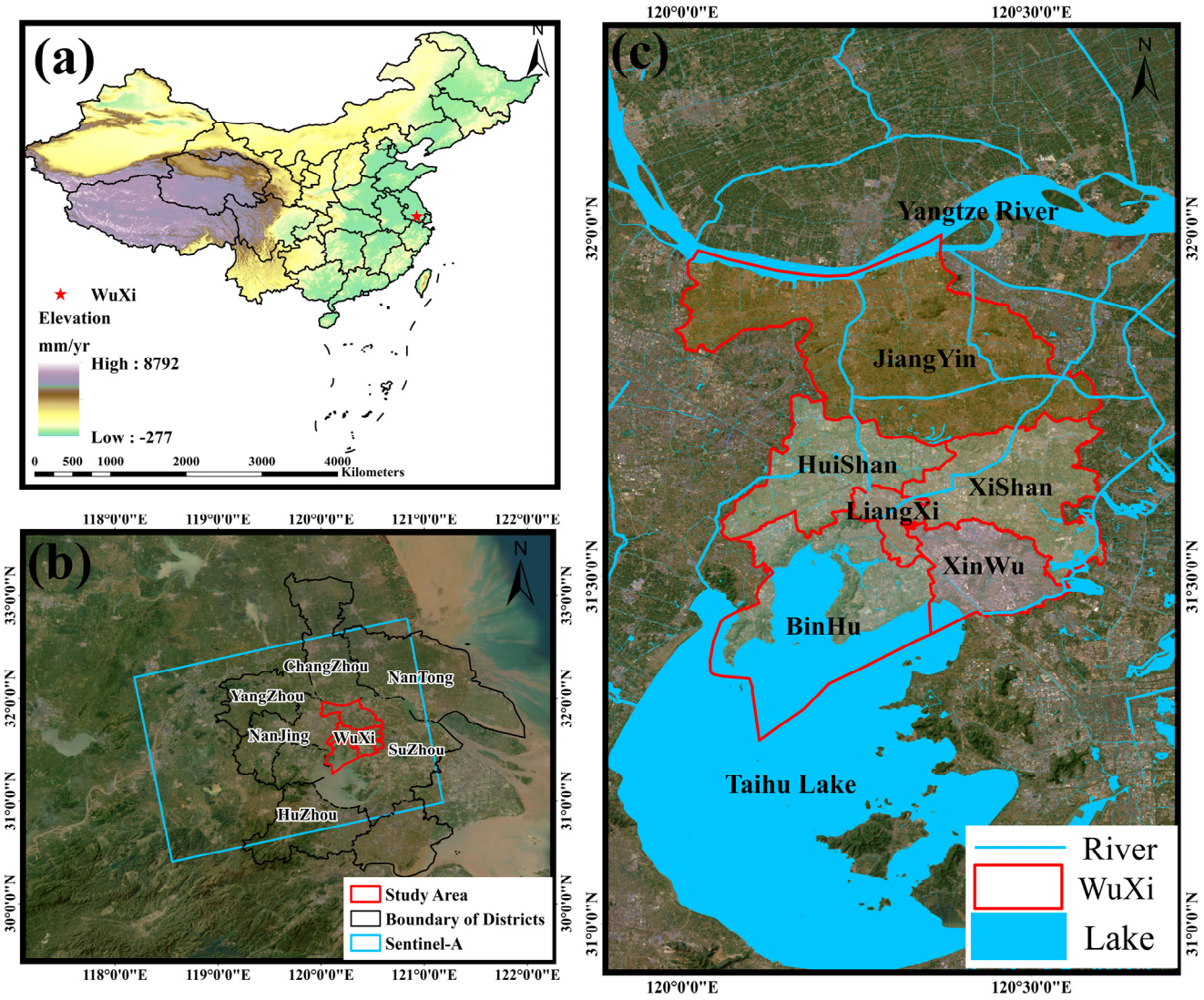

Figure 1. (**a**) The shapefile and digital elevation model map (DEM) of China. This map was provided by the China National Mapping and Resources Administration, representing the provincial maps of China. The red star represents Wuxi. (**b**) Geographical location of Wuxi. The blue rectangle illustrates the coverage of Sentinel-1A, and the red vectorgraph shows the study area. (**c**) Optical satellite image of Wuxi, wherein the red curve shows the administrative region of Wuxi, including Binhu (BH), Xinwu (XW), Xishan (XS), Liangxi (LX), Huishan (HS), and Jiangyin (JY).

3. Methodology

3.1. PS-InSAR Technique

In 2000, Ferretti et al. first proposed the concept of a "Permanent Scatterer (PS)" and the PS interferometry technique [34]. This technique utilizes multiple image data, extracts PS points based on the amplitude or coherence coefficient method, and then establishes a parametric equation that includes the average deformation rate, atmospheric delay phase, orbital residual error, and elevation error [35]. Through iterative calculations, the time-series information of surface deformation in the study area can be obtained, and the solution accuracy of this method can reach the millimeter level.

The processing flow of PS-InSAR is as follows: From N complex SAR images of the same scene, one image is selected as the master image, and the rest are slave images; the slave images are georeferenced with the master image, obtaining N-1 georeferenced SAR images; PS points are selected based on a set amplitude dispersion index threshold, and M interferometric pairs are generated [36]. The interferometric phase of each pixel in the interferometric pairs consists of multiple components, including the following:

$$\varphi = \varphi_0 + \varphi_{topo} + \varphi_{defo} + \varphi_{atm} + \varphi_{noise} \quad (1)$$

where φ is the total interferometric phase, φ_{defo} is the deformation phase, φ_0 is the phase on the reference ellipsoid, φ_{topo} is the topographic phase, φ_{atm} is the phase caused by changes in atmospheric conditions during the two radar acquisitions, and φ_{noise} is the random noise phase [37].

Using the known digital elevation model (DEM) data, differential interferometric processing is performed on the M interferometric pairs to obtain M differential interferograms. By establishing a phase difference model between adjacent PS points, the surface subsidence information is calculated. The phase difference between adjacent PS points in the i-th differential interferogram can be expressed as follows [38]:

$$\Delta\varphi_i = \frac{4\pi}{\lambda} T_i \Delta v + \frac{4\pi B_i^{\perp} \Delta\varepsilon}{\lambda R \sin\theta} + \Delta\varphi_i^{res} \quad (2)$$

where Δv is the deformation velocity difference between two adjacent PS points; $\Delta\varepsilon$ is the phase difference caused by the elevation error; $B_i^{\perp}$ and T_i are the spatial baseline and temporal baseline of the i-th interferogram, respectively; λ is the radar wavelength; R is the distance from the sensor to the target; θ is the radar incidence angle; $\Delta\varphi_i^{res}$ is the residual phase, including the atmospheric delay phase, nonlinear deformation phase, and noise phase.

Ferretti et al.'s research showed that under the condition of the absolute value of the residual phase being less than π, the deformation velocity difference Δv and the elevation error $\Delta\varepsilon$ can be estimated by maximizing the phase coherence coefficient model of M interferograms, with the objective function as follows [39]:

$$\gamma = \left| \frac{1}{M} \sum_{i=1}^{M} (\cos \Delta wi + j \cdot \sin \Delta wi) \right| = maximum \quad (3)$$

where γ is the model coherence coefficient; j is the imaginary unit, i.e., $j = \sqrt{-1}$; and Δwi represents the difference between the observed phase and the fitted phase of the i-th interferogram, namely

$$\Delta wi = \Delta\varphi_i - \frac{4\pi}{\lambda \cdot R \cdot \sin\vartheta} \cdot B_i^{\perp} \cdot \Delta\varepsilon - \frac{4\pi}{\lambda} \cdot T_i \cdot \Delta v \quad (4)$$

Although the objective function is highly nonlinear and the observed phase exhibits wrapping phenomena, by solving for the maximum value of the model coherence coefficient, the unknowns Δw and Δv for each baseline can be determined within a predefined solution space, avoiding the unwrapping process. Using γ as the weight and applying the weighted least-squares method, the time-series deformation velocity v and elevation error ε of PS points on a sparse grid are solved from known reference points [40]. By removing the linear deformation component of the PS points, the nonlinear deformation component, atmospheric delay, and decorrelation noise are obtained. Based on the spatial and temporal frequency characteristics of each component, filtering techniques are employed to decompose the signals. Among them, the atmospheric delay appears as a low-frequency signal in the spatial domain and a high-frequency signal in the temporal domain, exhibiting strong instability. By applying a high-pass filter to the residual phase in the temporal domain and

a low-pass filter in the spatial domain, the atmospheric delay phase of each image relative to the master image is obtained [38].

3.2. PS-InSAR Data Processing

Given the large amount of SAR data, long time span, and wide geographical coverage used in this study, we divided the 100 images covering the Wuxi area into two groups for processing. One group was used for detailed year-by-year analyses, while the other was used for long-term trend analyses, aiming to better understand the surface deformation patterns in Wuxi. We divided the period from November 2015 to June 2023 into three time intervals. Figure 2 shows the temporal baseline distribution and time span of these intervals. The specific processing flow, shown in Figure 3, mainly included five parts: data collection and preprocessing, differential interferometry calculations, first-step inversion, second-step inversion, and geocoding.

1. The data collection and processing part mainly included downloading 100 Single-Look Complex (SLC) images from the Alaska Satellite Facility (ASF) website and 100 precise orbit data items from the European Space Agency (ESA) georeferenced with the images. We chose the VV polarization mode with stronger penetration over the VH polarization mode. Subsequently, ENVI/IDL technology was used for batch preprocessing on the downloaded images, including master image selection, master–slave image georeferencing, and digital elevation model (DEM) phase simulation, obtaining interferometric pairs with spatial baseline, temporal baseline, and Doppler centroid frequency baseline coherence coefficients [41].
2. The differential interferometry calculations mainly included interferometric phase calculation, Permanent Scatterer candidate (PSC) point selection, flat earth and topographic phase removal, and differential interferogram calculation [42]. Using the interferograms obtained in the first step, target points with good coherence were selected. By performing a spatiotemporal characteristic analysis on each phase component in the differential phase, two-dimensional regression and objective function optimization methods were used to solve for the linear components. The linear deformation components of the Permanent Scatterer (PS) points were removed from the original differential interferometric phase to obtain the residual phase components.
3. For the first-step inversion, we used the first inversion model to calculate the residual height and displacement velocity, processing complex interferograms. This method determines a certain number of "Persistent Scatterers (PSs)" and processes the pixels around each PS point. PS points must satisfy two conditions: first, they must be stable; and second, they can be detected with the Synthetic Aperture Radar (SAR) antenna through proper orientation [43].
4. Second-step inversion was the final step of our inversion process, using the linear model results from the previous step to estimate the atmospheric phase components, thereby removing the atmospheric delay phase φ_{atm} and noise phase φ_{noise}. Finally, the model of the final displacement velocity was fitted, and the displacement for each date was extrapolated.
5. The PS-InSAR results were then geocoded and output in both vector (shapefile) and raster formats. In this study, the Product Temporal Coherence Threshold was set to 0.85, retaining the most effective feature points while eliminating low-coherence points to ensure data accuracy.

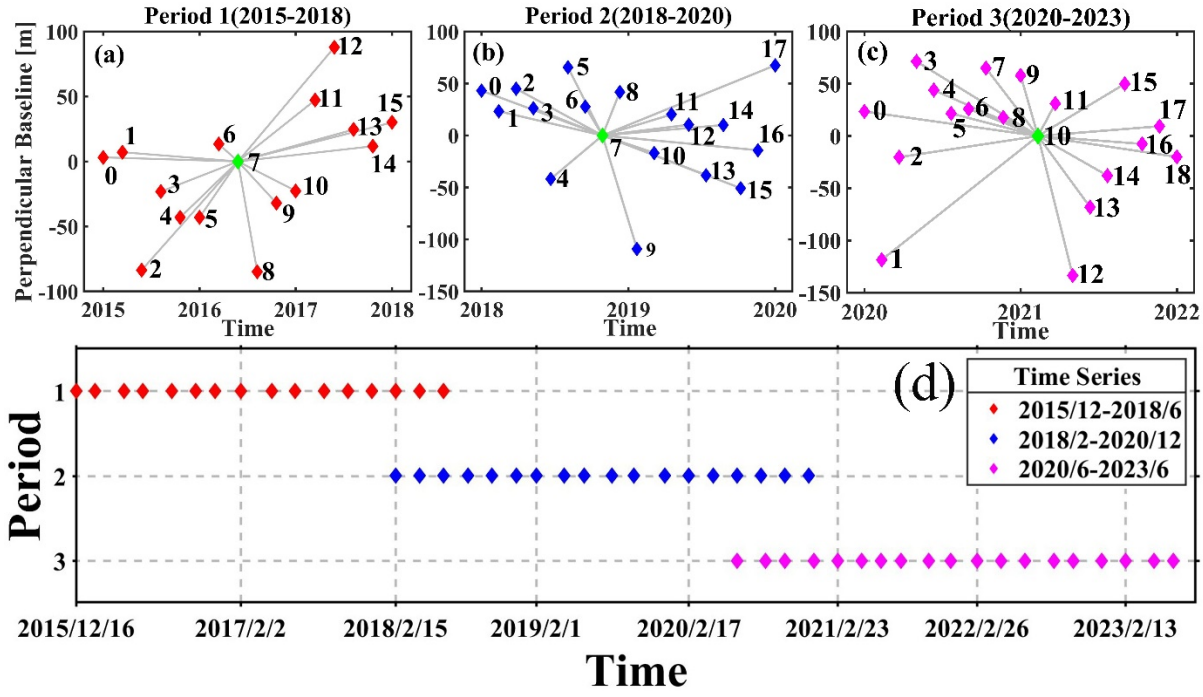

Figure 2. PS-InSAR spatiotemporal baseline graph for periods 1, 2, and 3, respectively (**a**–**c**). Time span of the three periods (**d**).

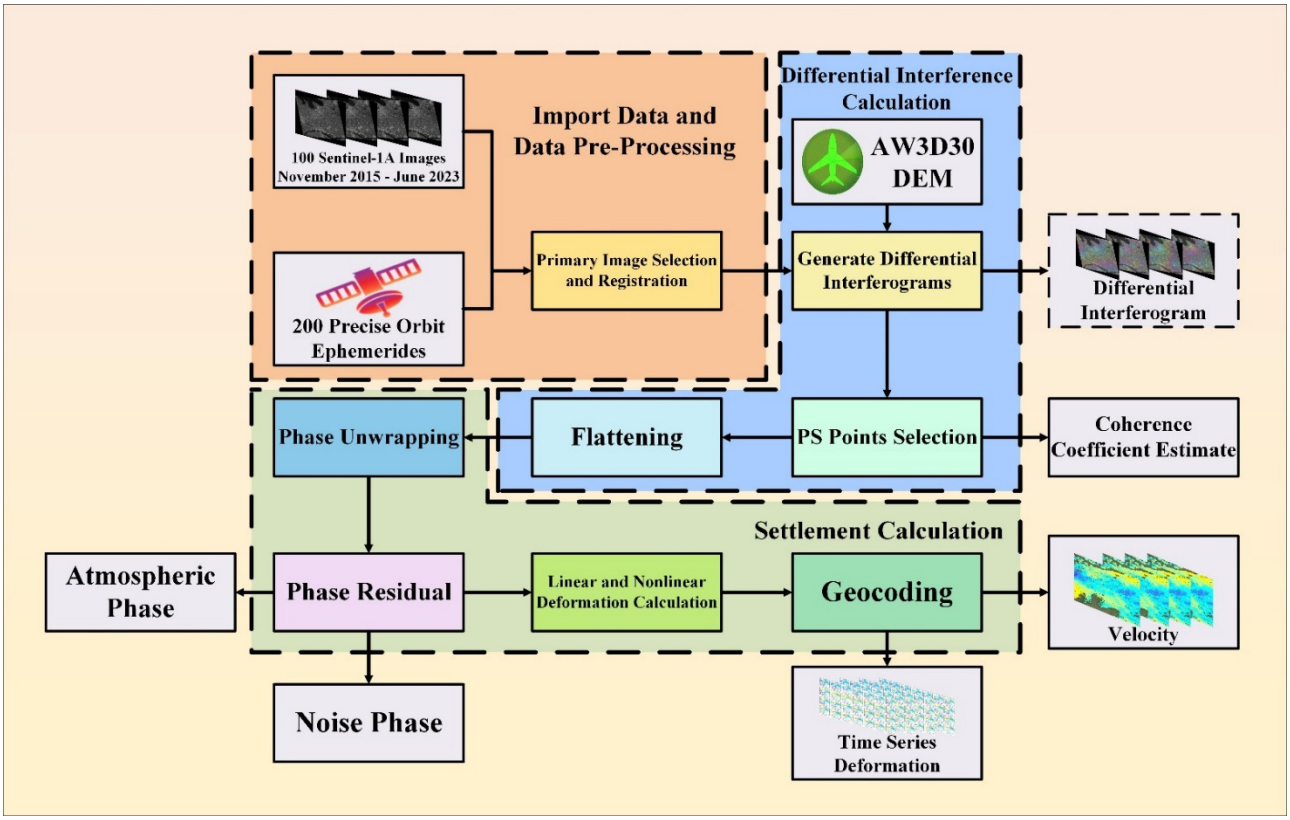

Figure 3. Data processing flow based on PS-InSAR.

3.3. Amplitude Factor Design

In finance, stock prices, futures, and exchange rates fluctuate over varying time periods, indicating that data volatility is not constant, but changes over time. Compared to

earlier models like ARMA, ARIMA, or ARCH [44], the error term variance in the GARCH model follows an autoregressive moving-average process, fully considering systematic error changes and more effectively capturing market volatility. Moreover, the GARCH model can effectively characterize volatility clustering, asymmetry, and long memory [45], and is regarded as one of the most mature models in current volatility research. Its basic equation is written as follows [46]:

$$\begin{cases} \mu_t = \sigma_t \varepsilon_t \\ \sigma_t^2 = \alpha_0 + \sum_{i=1}^{q} \alpha_i u_{t-i}^2 + \sum_{j=1}^{p} \gamma_j \sigma_{t-j}^2 \end{cases} \tag{5}$$

where σ_t^2 is the current volatility, representing the magnitude of conditional variance at time t; ε_t is an independent identically distributed unit of white noise with mean and unit variance values of zero; and μ_t is the current period residual.

In the established GARCH evaluation system, this study introduces the Amplitude Factor (AF) to measure the surface volatility of long-term time-series displacements in Wuxi. Here, σ_t^2 represents the current land surface deformation volatility and the mean of conditional variance reflects the historical volatility of surface deformation in the region. A higher mean of conditional variance implies a greater degree of fluctuation. Furthermore, the standard deviation, kurtosis, and median of conditional variance reflect the data stability, peak level, and central tendency, respectively [47]. To improve the accuracy of our research, we divided the study area into $0.005^\circ \times 0.005^\circ$ grid cells in ArcGIS and created 14,637 evaluation units. We input each grid cell's time-series displacement data into the GARCH model, calculated key statistical factors (mean, standard deviation, kurtosis, median), and assigned equal weights (as shown in Table 2). Then, we used the quantile method in ArcGIS to preliminarily classify values, ensuring equal evaluation units per category. We used the geometric interval method to set scores for each evaluation unit and assigned corresponding codes, with the highest value being 7 and the lowest being 1. According to the above criteria, we defined the score matrix S_i of the target evaluation unit as follows:

$$S_i = \begin{bmatrix} X_{11} & X_{12} & X_{13} & X_{14} \\ X_{21} & X_{22} & X_{23} & X_{24} \\ X_{31} & X_{32} & X_{33} & X_{34} \\ X_{41} & X_{42} & X_{43} & X_{44} \end{bmatrix}, \ i \in [1, n] \tag{6}$$

where i is the target evaluation unit, n is the total number of evaluation units, and X_{ab} is the corresponding element in Table 2 (a $\in [1, 4]$, corresponding to the indicators in the first column of Table 2; b $\in [1, 4]$, corresponding to the 4 score levels in the third column of Table 2).

The weight matrix Z of the statistical factors can be expressed as

$$Z = \begin{bmatrix} Z_1 & Z_2 & Z_3 & Z_4 \end{bmatrix}^T \tag{7}$$

$$\sum_{j=1}^{4} Z_j = 100\%, \ j \in [1, 4] \tag{8}$$

The constant parameter matrix C of the target unit is expressed as

$$C = \begin{bmatrix} 1 & 1 & 1 & 1 \end{bmatrix} \tag{9}$$

Then, the calculation formula for the Amplitude Factor (AF) value of the target unit is

$$AF_i = C \cdot (S_i \cdot Z), \ i \in [1, n] \tag{10}$$

Table 2. Comprehensive evaluation indicators for Amplitude Factors in the study area.

Indicator	Value	Score	Element	Weight (*Z*)
Mean (X_1)	0–2.2	1	X_{11}	25% (Z_1)
	2.2–2.9	3	X_{12}	
	2.9–3.9	5	X_{13}	
	>3.9	7	X_{14}	
Standard Deviation (X_2)	0–1.5	1	X_{21}	25% (Z_2)
	1.5–3.1	3	X_{22}	
	3.1–7.7	5	X_{23}	
	>7.7	7	X_{24}	
Kurtosis (X_3)	0–4.1	1	X_{31}	25% (Z_3)
	4.1–9.0	3	X_{32}	
	9.0–22.0	5	X_{33}	
	>22.0	7	X_{34}	
Median (X_4)	0–1.8	1	X_{41}	25% (Z_4)
	1.8–2.5	3	X_{42}	
	2.5–3.2	5	X_{43}	
	>3.2	7	X_{44}	

4. Results

4.1. Annual Results of Rebound Deformation in the Wuxi Area

After processing 100 SAR images using the method introduced in Section 3.2, we obtained the surface deformation velocity field of the Wuxi area from November 2015 to June 2023. This study took one year as its research time interval, allowing an error of plus or minus two months. Figure 4 shows the surface deformation velocity map of the Wuxi area obtained using the PS-InSAR technique, where positive values indicate uplift and negative values indicate subsidence. The velocity map is overlaid on a satellite image of the Wuxi area obtained from the Mapbox platform.

As shown in Figure 4, the Wuxi area does not exhibit a consistent subsidence or uplift trend in the year-by-year analysis, but there are significant fluctuations, mainly concentrated in the BH, XS, and LX regions. The BH region shows a trend of large changes initially, followed by gradual stabilization, and then large changes again, with poor stability of surface deformation in recent years. The XS region is located between regions XW and JY, with its eastern part mainly consisting of villages and towns, showing good stability, while the western part is an urbanized area, with more evident surface deformation compared to the eastern part. The LX region is located in the central part of the main urban area of Wuxi City, and as time progresses, the volatility of its surface deformation becomes more evident.

The BH region is located in the Binhu District of Wuxi City. Since the Jiangsu Provincial People's Congress proposed the "Decision on Prohibiting Groundwater Extraction in Suzhou, Wuxi, and Changzhou Areas within a Time Limit" [48] in 2000, Wuxi City has comprehensively banned groundwater extraction since 2005. After a long period of development, the groundwater in the area has been fully replenished. Therefore, compared with previous studies [29], the surface subsidence occurring within the study area of this paper has been significantly alleviated. However, instability still exists in the area. The Lingshan Grand Buddha Scenic Area on its west side experienced a certain degree of subsidence in 2016, followed by significant uplift in 2017 and 2018, whereas after 2020, it experienced subsidence of varying degrees again. The Hongsha Bay area on its southeast side also experienced significant surface deformation in 2016–2017, followed by a smoothing trend, but in the first half of 2023, it experienced relatively evident surface subsidence again.

The XW region is located in the Xinwu District, southeast of Wuxi City. According to the time-series subsidence rate map, the annual average (uplift/subsidence) rate in this area ranged from −5.19 to 1.93 mm/year, with few changes, but evident fluctuations. According to the "Adjustment Plan for the Overall Land Use Planning of Xinwu District, Wuxi City (2006–2020)" [49] issued by the People's Government of Xinwu District, Wuxi

City strictly restricted urban and industrial construction in Xinwu District. From 2014 to 2020, the urban construction area increased by only 2.23%, so there was no significant subsidence in the area.

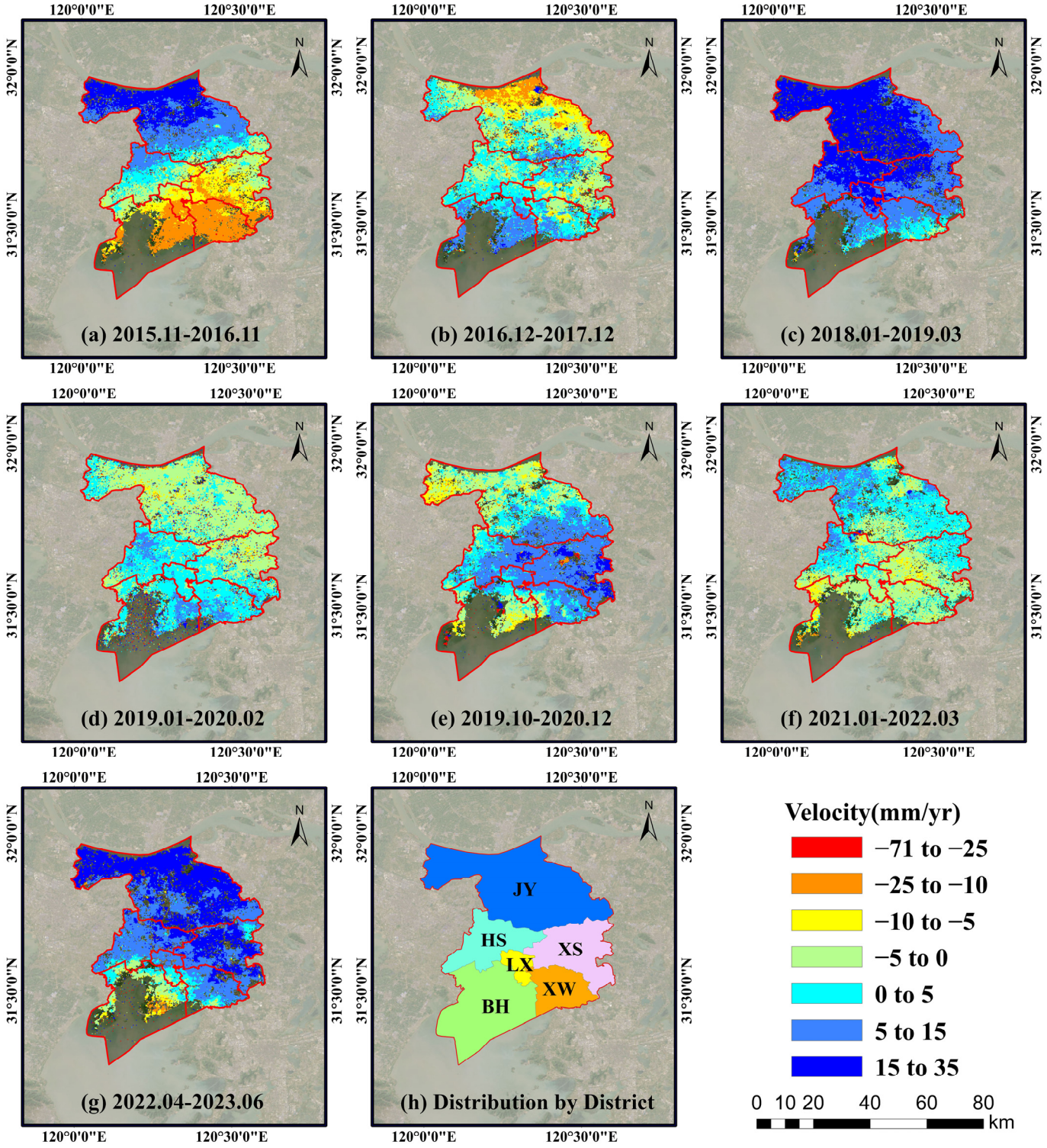

Figure 4. (**a**–**g**) Surface deformation rate maps of the Wuxi region from 2015/11 to 2023/06 (with a positive and negative difference of no more than 2 months) obtained by using PS-InSAR. Positive values represent surface uplift, while negative values represent surface subsidence. (**h**) The specific distribution of administrative regions in Wuxi City.

The JY region, within Jiangyin City under Wuxi City's jurisdiction, saw significant development following the 2012 approval of the "Jiangyin City Master Plan (2011–2030)" by the local government [50]. This plan aimed to foster rapid urbanization and enhance central urban area construction, while strictly safeguarding ecological assets like rivers, essential farmland, and riverside ecological wetlands, and conserving resources such as land and groundwater. These strategies has propelled Jiangyin City's swift progress in recent years, moderating the surface deformation fluctuations. From 2015 to 2023, the southern townships and villages saw no notable surface subsidence. However, the northern riverside area, constituting Jiangyin's primary urban zone, experienced the most pronounced deformation fluctuations in our study. Its proximity to the Yangtze River significantly influences surface changes through pore-confined water levels, a focal point of the discussion in Section 5.

4.2. Long-Term Results of Surface Deformation in Wuxi Area

The velocity of surface deformation in the Wuxi area from 2015 to 2018, 2018 to 2020, and 2020 to 2023 measured through the PS-InSAR method are shown in Figure 5. The positive values in the figure indicate ground uplift, while the negative values indicate land subsidence.

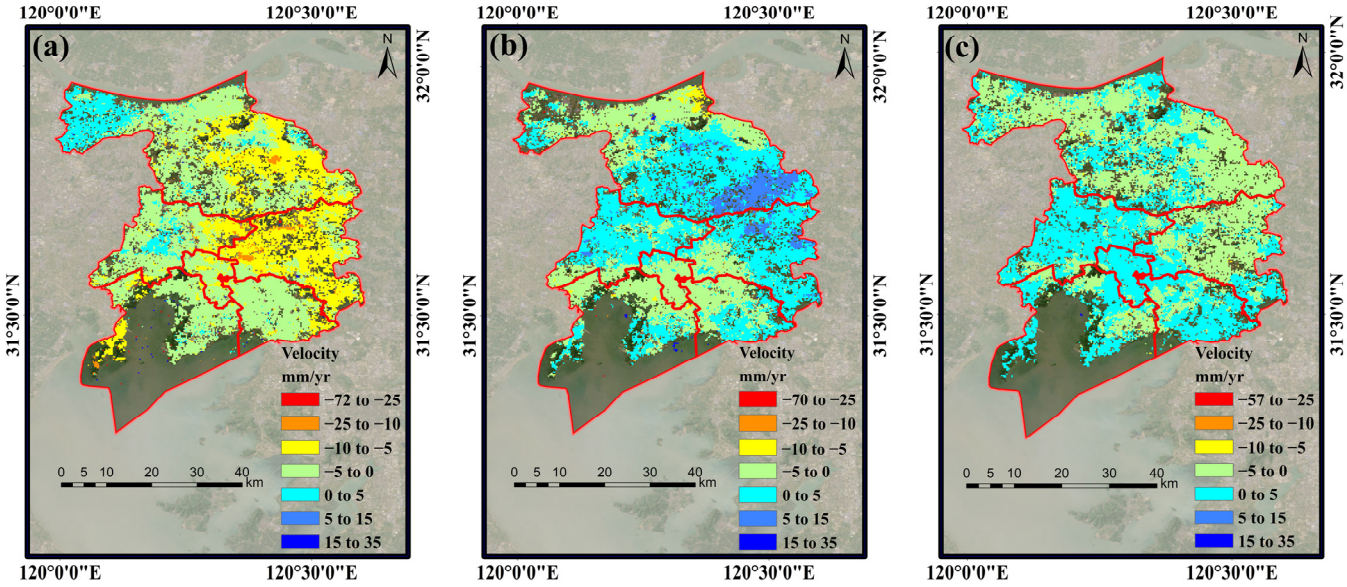

Figure 5. Surface deformation changes in Wuxi over different time spans. (**a**) Surface deformation rate in the LOS direction in Wuxi from December 2015 to June 2018; (**b**) surface deformation rate in the LOS direction in Wuxi from February 2018 to December 2020; (**c**) surface deformation rate in the LOS direction in Wuxi from June 2020 to June 2023.

The period from December 2015 to June 2018 is represented by a set of SAR images containing 16 scenes. Figure 5a shows the surface deformation velocity map along the LOS direction for this period. From 2015 to 2018, a total of 5,652,151 PS points were obtained, with deformation velocities ranging from −23.97 mm/year to 29.09 mm/year and an average of 6.52 mm/year. In total, 90.3% of the surface deformation velocities in the study area are between −6.02 mm/year and 11.01 mm/year. During this period, the surface deformation in the Wuxi area generally shows an uplifting trend, with some areas remaining unchanged. The Huishan District in western Wuxi exhibits a significant large-scale uplift, with average annual uplift rates between −2.47 mm/year and 18.78 mm/year. Additionally, several key deformation zones with uplift rates exceeding 12 mm/year appear along the Yangtze River in the northern Jiangyin City. Compared with the results of the previous segmented study, the subsidence zone in the south in 2016 partially overlaps with the uplift zone in the south in 2017, and the uplift zone in the north in 2016 partially

overlaps with the subsidence zone in the north in 2017. Therefore, in these two overlapping areas, the surface deformation underwent a certain neutralization effect. Furthermore, in the first half of 2018, the overall area experienced a significant uplift, causing the overall deformation effect to match the aforementioned image results.

The period from February 2018 to December 2020 is represented by a set of SAR images containing 18 scenes. Figure 5b shows the surface deformation velocity map along the LOS direction for this period. From 2018 to 2020, a total of 2,544,221 PS points were obtained, with deformation velocities ranging from −40.03 mm/year to 22.90 mm/year and an average of 0.29 mm/year. Compared to the period from 2015 to 2018, the overall subsidence trend is relatively gentle, with no large-scale obvious uplift or subsidence. By comparing the three annual average velocity maps from 2018 to 2020 in Section 4.1, it can be seen that although the Binhu District in southwestern Wuxi and the Liangxi District near the central area experienced large-scale subsidence in 2020, they both experienced slow uplift in 2018 and 2019; the subsidence and uplift had a neutralization effect, resulting in a stable changing trend in the long-term time series. Moreover, the Xinwu District in southeastern Wuxi, the Xishan District in the central area, and the junction area within Jiangyin City, although experiencing significant uplift in certain specific years, show a stable trend in the remaining years; this implies that the uplift effect was weakened, resulting in a stable trend in the overall deformation.

The period from June 2020 to June 2023 is represented by a set of SAR images containing 19 scenes. Figure 5c shows the surface deformation velocity map along the LOS direction for this period. From 2020 to 2023, a total of 3,536,105 PS points were obtained, with 88.53% of the PS points having deformation velocities between −25.98 mm/year and 30.01 mm/year. Unlike the significant uplift trend from April 2022 to June 2023, the surface deformation during this study period was relatively small. The main reason for this is that during the period from June 2020 to March 2022, some areas experienced continuous small-scale subsidence, thus weakening the subsequent uplift trend.

For this section of our study, we conducted mathematical statistical analyses on the deformation information obtained through the PS-InSAR technique for two time periods. To further understand the time-series changes in the deformation velocity, we separately counted the surface subsidence and uplift information, and the statistical results are shown in Figure 6.

According to the subsidence statistics chart, from 2015 to 2023, the subsidence rate in Wuxi shows a decreasing trend. From 2015 to 2018, PS points with subsidence rates between 0 and 4 mm/year account for 62.16% of all subsidence points, and this proportion reaches 92.97% in 2018–2020 and exceeds 95% in the last study period. However, for PS points with subsidence rates above 4 mm/year, the number in the first time period far exceeds the latter two time periods, and PS points with subsidence rates exceeding 8 mm/year rarely appear after 2018. From the uplift statistics data, the uplift in the Wuxi area shows a fluctuating trend of increasing first and then decreasing. In 2018–2020, PS points with uplift rates between 0 and 4 mm/year are fewer than those in the two time periods before and after, while PS points with uplift rates above 4 mm/year appear more than in the two time periods before and after. This also indirectly reflects the periodic changing trend of the surface deformation in the Wuxi area.

In this study, we obtained data on the surface deformation of the Wuxi area from 2015 to 2023. To study the characteristics of early surface deformation and compare them with our results, we summarized other surface subsidence studies conducted in the Wuxi area in the past, which are presented in Table 3.

From 2004 to 2011, Wuxi City formed two major subsidence areas: Jiangyin and Xishan. Lu et al. analyzed the surface subsidence in Wuxi City from 2004 to 2017 and found that from 2004 to 2011, large subsidence funnels appeared in the southern part of Jiangyin City and the Huishan District bordering Jiangyin City, with a maximum subsidence rate exceeding 20 mm/year [29]. After 2011, InSAR results indicated that the subsidence areas in Jiangyin City and Huishan District tended to flatten, and the overall subsidence expanded

to the southeastern part of Wuxi [52]. After 2015, the subsidence in the junction area of Xishan District and Jiangyin City in Wuxi City showed a slowing trend, and relatively obvious subsidence areas appeared in Xinwu District and Binhu District. Although previous studies [51] used different data and methods to monitor surface deformation, they were able to identify similar subsidence/uplift areas and surface deformation rates. Compared with the results of previous studies, the spatiotemporal distribution characteristics of the subsidence areas detected in the present study are basically consistent [33].

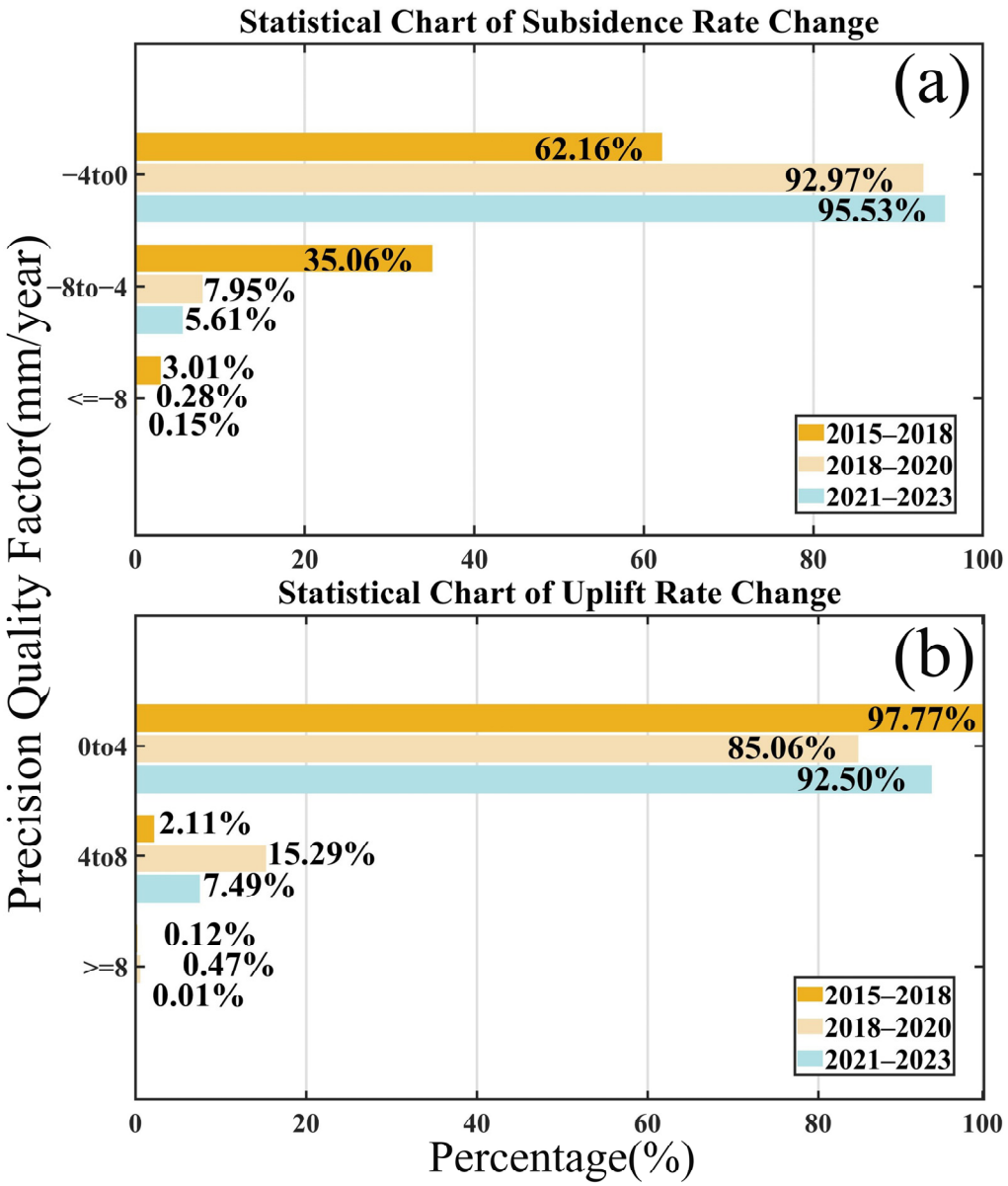

Figure 6. Statistical charts showing the changes in deformation information at all PS points in the Wuxi region from 2015 to 2023. (**a**) PS points of the subsidence part, where brown stripes represent 2015–2018, light-orange stripes represent 2018–2020, and nattier-blue stripes represent 2021–2023. (**b**) PS points of the uplift part, where the different colored stripes represent the same years as those they represent in (**a**).

Table 3. Summary of previous studies on land subsidence in Wuxi.

Reference	Method	Datasets	Main Subsidence Areas	Deformation Rates
Yang et al. [33]	PS-InSAR	23 ENVISAT ASAR images (November 2007 to April 2010) 42 Sentinel-1A images (January 2018 to June 2021)	Huishan District, Jiangyin City, Xishan District	−25 to 5 mm/year (2007–2010) −5 to 5 mm/year (2018–2021)
Lu et al. [29]	SBAS-InSAR	68 ALOS PALSAR images (February 2007 to February 2011)	Huishan District, Jiangyin City, Xishan District	−40 to 10 mm/year
Li et al. [51]	PS-InSAR	52 Sentinel-1A images (January 2019 to December2019)	Xishan District, Jiangyin City	−10 to 10 mm/year
Fan et al. [52]	MCTSB-InSAR	25 RADARSAT-2 images (February 2012 to January 2016)	Xishan District, Jiangyin City,	−25 to 5 mm/year
Ouyang et al. [53]	PS-InSAR	25 Sentinel-1A (October 2018 to October 2020)	Binhu District, Xinwu District, Xishan District	−14 to 10 mm/year

4.3. Accuracy Verification of Rebound Results

Using 100 Sentinel-1 SAR images covering the Wuxi area, surface deformation information from November 2015 to June 2023 was obtained via the PS-InSAR technique. After three data processing iterations, over 117,427 PS points were obtained. We calculated the amplitude dispersion index (i.e., the ratio of mean to standard deviation) for all PS points as a precision quality factor, assessing the internal precision quality of the obtained surface deformation information.

As shown in Figure 7a, 94.38% of the total points had a precision quality better than 7.0 mm/year. Similarly, 96.89% of the total points in Figure 7b and 94.41% in Figure 7c had precision qualities better than 7.0 mm/year.

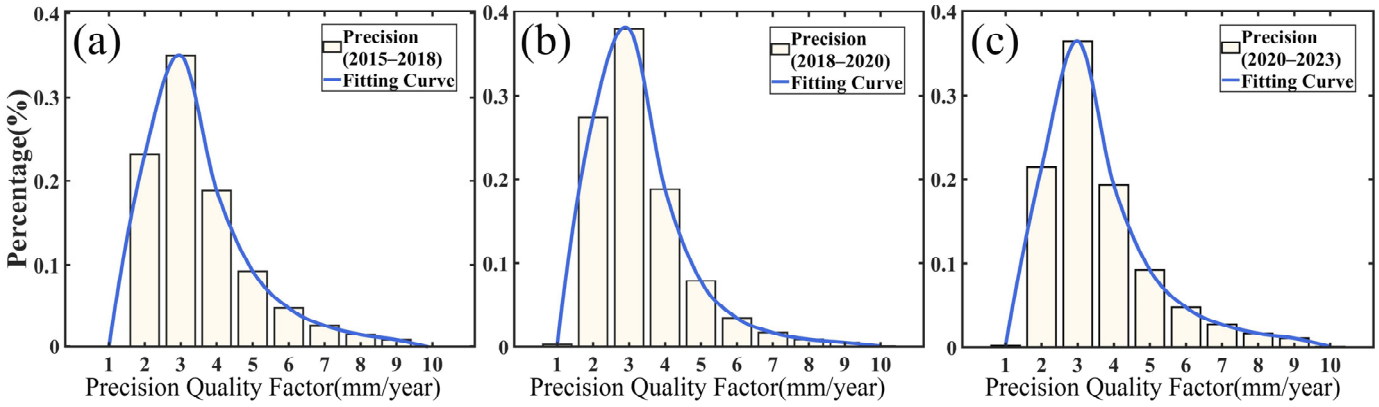

Figure 7. Precision quality factor statistics regarding the deformation information of PS points in the Wuxi area acquired using the PS-InSAR method. (**a**) Precision quality factor statistics of deformation information in 2015–2018; (**b**) precision quality factor statistics of deformation information in 2018–2020; (**c**) precision quality factor statistics of deformation information in 2020–2023.

These results indicate that using ascending Sentinel-1 data with IW polarization to obtain surface information in Wuxi, combined with PS-InSAR processing and analysis, results in very high precision and reliability. Furthermore, cross-validation methods were employed to verify this method's accuracy—details on this are provided in the Supplementary Materials.

5. Discussion

5.1. Time-Series Analyses of Characteristic Points

For this section, to better analyze the spatial distribution characteristics of surface rebound changes in Wuxi City, we randomly selected six different characteristic points distributed throughout Wuxi City to conduct a detailed analysis. The method for selecting these characteristic points was as follows: first, the location of each characteristic point was determined; then, a circle with a radius of 500 m centered on these points was drawn, designating the characteristic area. The temporal cumulative deformation of the characteristic points is shown in Figure 8a, with their specific distribution locations illustrated in Figure 8b.

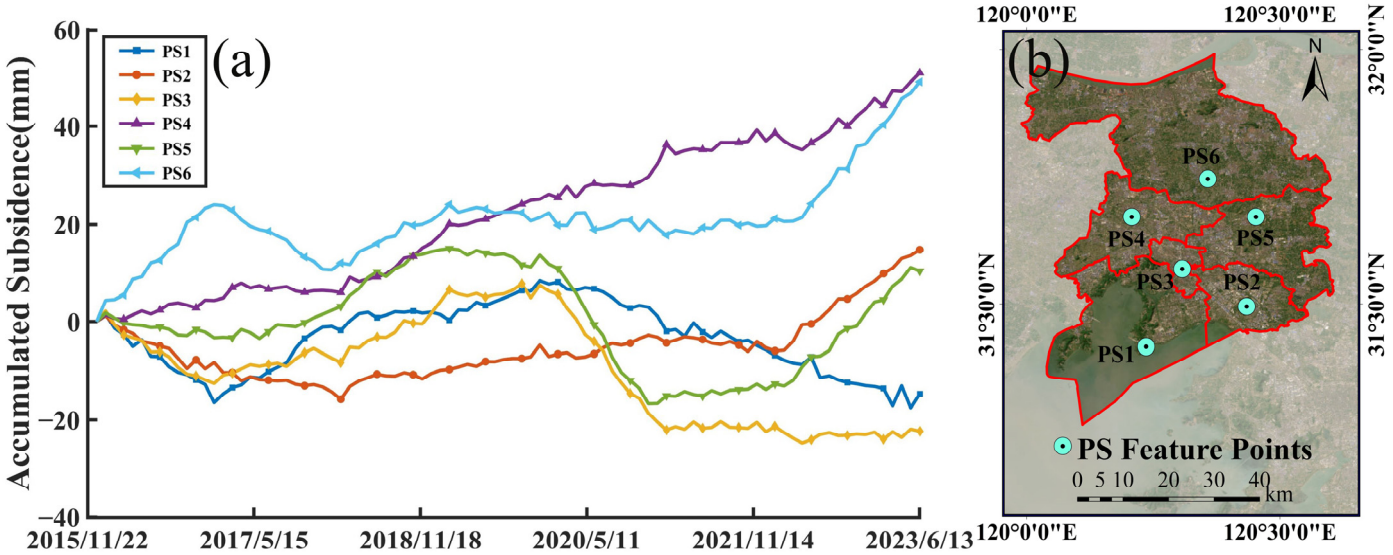

Figure 8. Time series of deformation for the PS points labeled PS1–PS6 (**a**). Location of different PS characteristic points (**b**).

PS1 is located near Hongsha Bay in the Binhu District, close to the Taihu Lake area. This area exhibited continuous small-scale fluctuation changes, with the maximum cumulative uplift being 8.55 mm and the maximum cumulative subsidence being −16.62 mm. Due to changes in the water level of Taihu Lake, which lead to variations in the confined water level in this area, water level changes were the main factor causing these regional variations.

PS2 is located in the Shuofang Airport area of the Xinwu District. This area showed a trend of slight subsidence followed by slow uplift. The area has many new technology and industrial parks, the construction of which increased the compressive stress on the surface, causing subsidence; this was followed by a slow rebound due to substantial groundwater recharge [54].

PS3 is located near the Liangxi District People's Government. Prior to 2021, this point experienced wide-ranging fluctuation changes, but following the issuance of the "Fourteenth Five-Year Plan for National Economic and Social Development of Liangxi District, Wuxi City and the Vision for 2035" [55], Liangxi District strengthened its ecological civilization system construction, strictly controlled urban development boundaries, and scientifically managed the relationship between urban development and land resource utilization; therefore, in subsequent periods, this area showed a stable trend.

PS4 is located near the Huishan District railway station. There were no significant fluctuation changes here, showing a trend of a slow uplift.

PS5 is located near the Xibei Town People's Government in Xishan District. This area has many factories, such as vehicle parts, railway parts, and plastics factories, leading to a significant proportion of the water in this area being used for industrial purposes compared

to other areas; and, since 2018, the region has focused on creating major industrial projects and extensive construction, leading to poor surface stability in this area.

PS6 is located near Xiangshan Village, at the junction of the southern part of Jiangyin City and Xishan District. The figure shows that this area exhibits a weak fluctuation, with an overall trend toward stability. After April 2022, this region experienced a significant uplift, related to increased precipitation and groundwater changes, which will be discussed in detail in the following section of this paper.

Overall, the fluctuation changes in the Wuxi area are uneven. This situation is mainly related to groundwater, which will be focused on in the next section.

5.2. Changes in Surface Deformation and Groundwater Level

In the groundwater layer, groundwater extraction leads to a decreased water level and correspondingly reduces the pore water pressure in the aquifer and surrounding relatively impermeable layers. Per the effective stress principle, the total stress in soil caused by overburdening is jointly borne by the pore water and soil particle skeleton. The portion borne by water is called the pore water pressure P_W, which does not cause soil compression and is thus also called neutral pressure; the portion borne by the soil skeleton directly causes upper-layer compression and is called effective stress P_S. The sum of these two equals the total stress [56]. Assuming that the internal soil stress remains unchanged during water extraction, decreased pore water pressure inevitably leads to an equal increase in effective stress, which compresses the soil layer. Under lower-stress conditions, sand layers exhibit low compressibility and mainly demonstrate reversible elastic deformation, while clay layers exhibit much higher compressibility and primarily undergo permanent inelastic deformation. Therefore, under lower-effective-stress conditions, cohesive soil layer consolidation dominates the land subsidence, while sand layer expansion and rebound are crucial during water level recovery [57]. The effective stress schematic is shown in Figure 9, wherein soil particles above the groundwater level are not displayed.

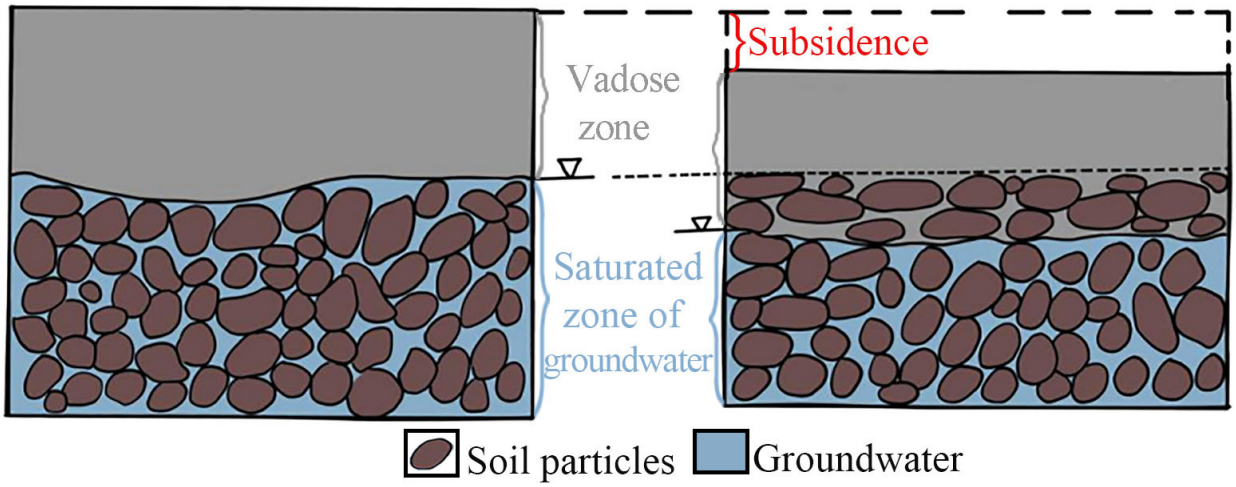

Figure 9. Schematic diagram of the effective stress principle. The decline in groundwater levels results in increased downward stress on the particles originally filled with groundwater, causing them to be compressed and leading to land subsidence.

For this section, we selected groundwater level data from six local confined aquifer groundwater-monitoring wells from January 2018 to December 2021, using monthly intervals to form time series of groundwater level changes, with the well locations being distributed as shown in Figure 10G. InSAR elevation time series were derived from all PS pixels within a 200 m radius around each observation well, and LOS direction displacement data (red line) and water level changes (blue line) were normalized, comprehensively compared, and ultimately plotted, as displayed in Figure 10A–F.

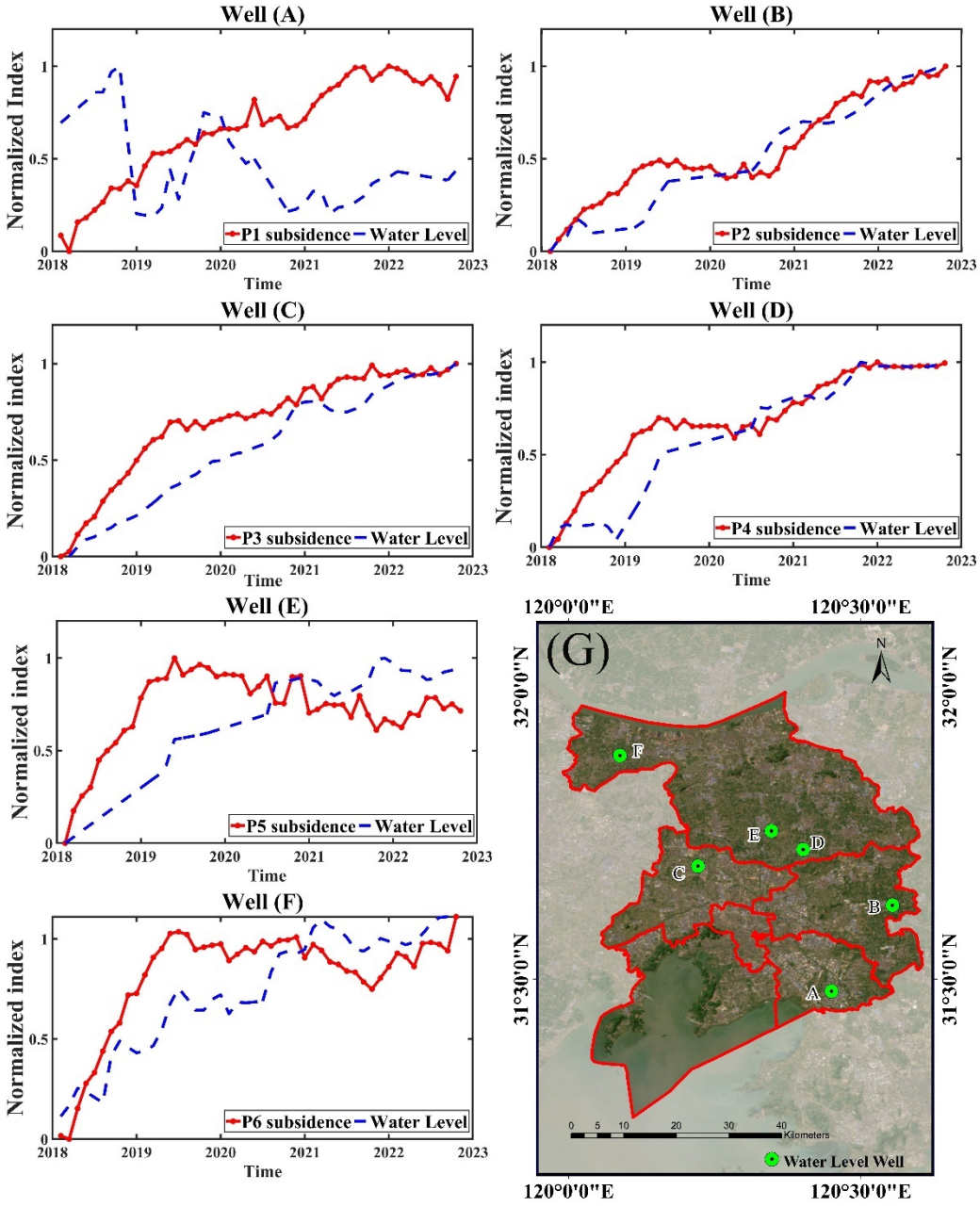

Figure 10. The spatiotemporal relationship between water level changes and InSAR inversion deformation. (**A**–**F**) Changes in groundwater level for wells (**A**–**F**), respectively. (**G**) Distribution of the monitoring wells.

The stratigraphic structure in the Wuxi area is relatively complex, with thick sand and gravel-bearing sand layers, while the clay layers are thin and unevenly distributed [58]. According to the above figures, it can be observed that all areas near the wells exhibit a slow rebound trend, which is closely related to the expansion and rebound of the sand layers. Furthermore, the changes in confined water levels have a high correlation with the InSAR-derived surface elevations. We employed the GRA method to calculate the relationship between the elevation and water level, obtaining GRA values of 0.52, 0.71, 0.61, 0.75, 0.57, and 0.65 for wells (A), (B), (C), (D), (E), and (F), respectively. Well (A) is located in the Shuofang Economic and Trade Service Center, Binhu District, Wuxi City, while well (E) is situated in Huangtang Village, Jiangyin City, one of the county-level cities in Wuxi. From January 2018 to December 2022, the cumulative displacement components in the LOS direction for wells (A) and (E) were 14.29 mm and 12.59 mm, respectively,

while the groundwater level changes were −0.82 mm and 10.85 mm, respectively. The groundwater level changes in well (E) are consistent with the LOS direction displacement changes, while well (A) shows significant differences. Moreover, the trends of displacement changes for wells (A) and (E) have low correlations with the water level changes. The reasons for these differences are as follows: (1) the local soil and geological conditions of the two wells are different, resulting in varying impacts of confined water on the surface deformation; (2) the influence of groundwater level changes on surface deformation has a certain lag, and for some areas, the impact is not immediately apparent but has a certain delay; (3) the groundwater observation accuracy of well (E) is insufficient, with some abnormal values; (4) surface subsidence is affected by multiple factors, with groundwater being only one of them, and the combined effects of other aspects lead to suboptimal fitting results. Well (B) is located in Yangjian Town, Xishan District, while well (D) is situated in the Wenlin Community Service Center, Jiangyin City, both located in the border area between Xishan District and Jiangyin City. From Figure 10, it can be seen that the changing trends of the surface deformation and water level for these two wells are generally similar; when the groundwater level rises, the surface undergoes uplift and rebound, and when the groundwater level decreases, the ground subsides. Their gray relational degree indices both exceed 0.7, indicating that changes in confined aquifer water levels are the main cause of surface deformation in this subsidence area. Well (C) is located on Qianzhou Street, Huishan District, while well (F) is situated on Lingang Street, Jiangyin City. From Figure 10, it can be observed that these two areas experienced significant uplift in 2018, with well (C) uplifting by 24.60 mm and well (F) uplifting by 23.45 mm. The groundwater level correspondingly increased, altering the surface flotation effect. Water level rises may relate to artificial groundwater recharge and natural precipitation, as detailed in Section 5.3.

Additionally, as seen in Figure 10B–F, from early 2018 to mid-2020, rising groundwater levels led to rapid surface uplift with a clear lag effect (or groundwater residence time) between the two. Determined using the time-lagged cross-correlation method [59], during this period, the groundwater in most areas had a residence time of 2–4 months. After the surface uplift (rebound) reached a certain level, this effect gradually weakened or disappeared.

Overall, surface subsidence deformation closely relates to confined aquifer water. Recent government attention and legal protection has enabled artificial groundwater recharge to effectively suppress the surface subsidence in Wuxi. However, reasonable limits should be set for artificial recharge processes to avoid excessive rebound from overly high recharge rates. In the future, ground-based SAR imaging radar devices could be deployed around water wells, combined with geodetic surveying for real-time subsidence monitoring, stabilizing the surface.

5.3. Impact of Precipitation on the Surface Flotation Effect

According to the "Notice on Carrying Out Systematic and Comprehensive Demonstration Work for the Construction of Sponge Cities" issued by the Ministry of Finance, Ministry of Housing and Urban-Rural Development, and Ministry of Water Resources, Wuxi City was designated as one of the first batches for sponge city construction demonstrations in China in 2021 [60]. As one of the key elements of a sponge body, soil is directly affected by precipitation. Previous studies have shown that rainwater infiltration increases soil moisture content and reduces soil porosity and bulk density [61]. This implies that when precipitation increases, the soil behaves like a water-saturated sponge, undergoing uplift and elastic rebound while indirectly recharging the groundwater.

Wuxi is located in the humid subtropical monsoon climate zone of North Asia, bordering the Yangtze River to the north and Taihu Lake to the south, characterized by abundant precipitation and concurrent rain and heat. This study collected monthly average precipitation data from January 2018 to December 2021 provided by the official website of the China Meteorological Administration (https://weather.cma.cn/ (accessed on 7 December 2023)) and divided the Wuxi area into five latitudinal zones from north to south

(N1:31°51′36″–31°59′24″; N2:31°43′12″–31°51′36″; N3:31°35′24″–31°43′12″; N4:31°27′36″–31°35′24″; N5:31°19′48″–31°27′36″), with the longitude ranging from E119°41′13″ to E120°39′58″.

As shown in Figure 11, the amounts of precipitation in these five latitudinal zones are very similar, with more precipitation in the south and less in the north, consistent with the meteorological conditions of the humid south and arid north in China. Therefore, for this study, we averaged the monthly precipitation of these five latitudinal zones and compared them with the four characteristic regions in Figure 12b to analyze the impact of precipitation on the surface flotation effect.

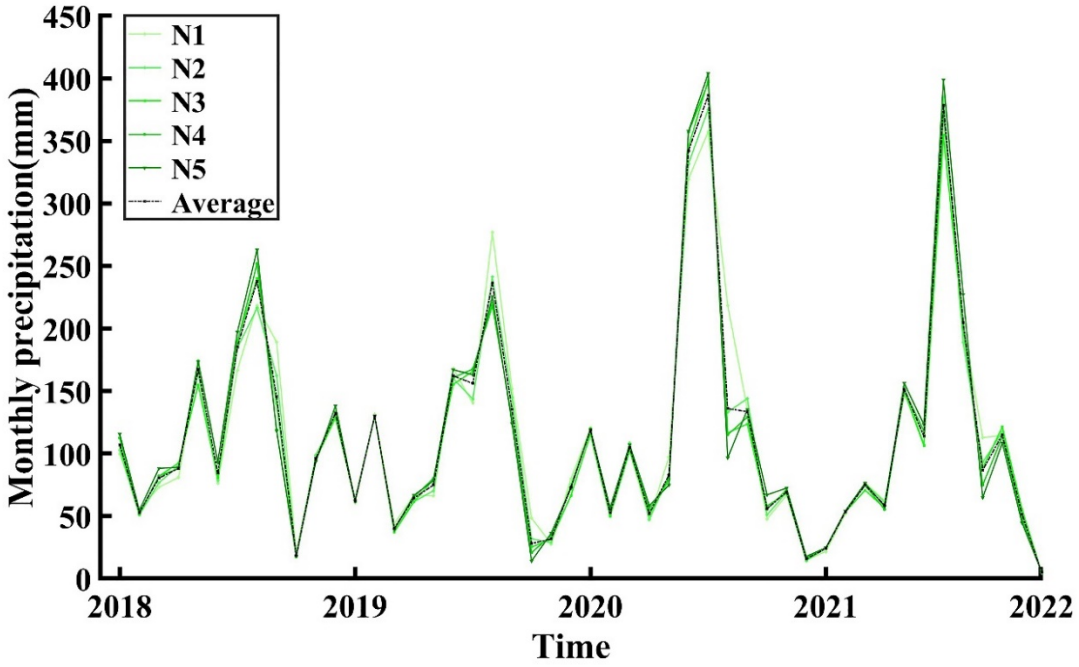

Figure 11. Comparative analysis of precipitation in 5 latitudinal zones.

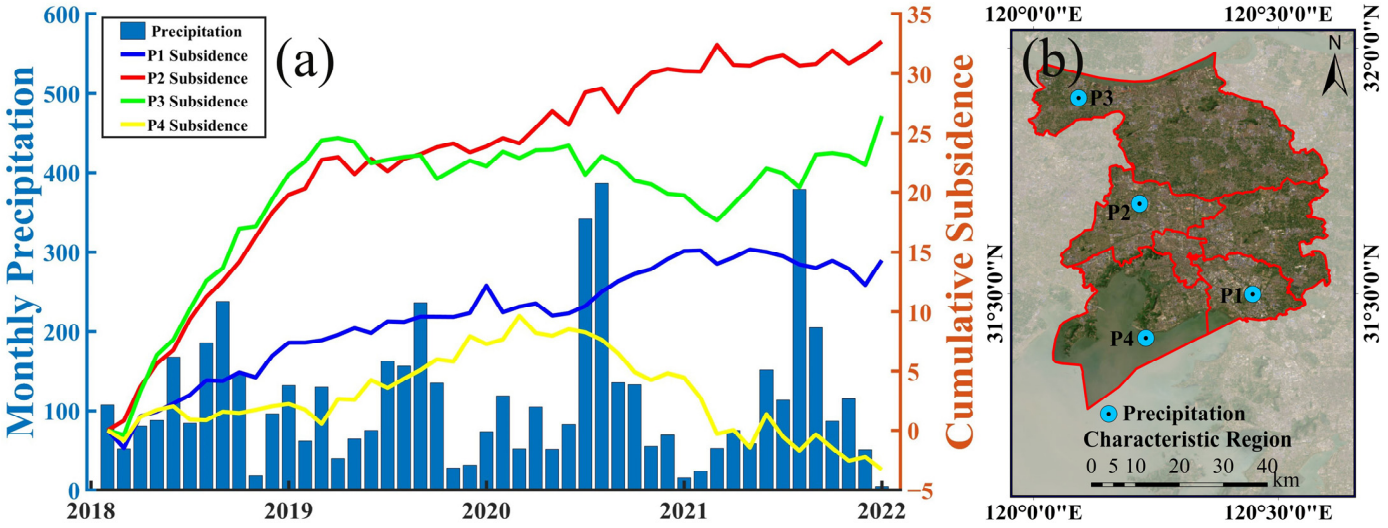

Figure 12. (**a**) The impact of precipitation on the surface buoyancy effect. (**b**) Regional distribution of precipitation characteristics.

From Figure 12a, it is observed that from January 2018 to early 2020, precipitation was concentrated from May to September each year, with less precipitation in other months; after 2020, precipitation was concentrated from June to August each year, with the precipitation

during this period far exceeding the previous flood season precipitation, while in other dry seasons, precipitation was reduced compared to the previous period. This indicates that the precipitation distribution from 2020 to 2022 was concentrated and high in volume. Overall, due to the increased precipitation during the flood season from 2020 to 2022, the annual precipitation after 2020 was greater than that before 2020. P1 is located near Shuofang Airport in Xinwu District, and P4 is located in the Hongsha Bay area of Binhu District. The common feature of both locations is that during seasons with increased precipitation, the surface experienced an uplift, while during seasons with less precipitation, a subsidence trend occurred. This indicates that precipitation and surface elevation exhibit a partial linear correlation, reflecting the surface flotation effect caused by precipitation infiltration. However, during a few periods, when precipitation increased, the surface did not exhibit a corresponding response, indicating that surface subsidence is related to multiple factors, with precipitation being a secondary factor at this time. P2 is located in the Qianzhou Street area of Huishan District, near well (C) described in Section 5.2; P3 is located on Lingang Street, near well (F) discussed in Section 5.2. We found that although both the groundwater and surface levels in these two regions exhibited a certain degree of increase in 2018, the precipitation in 2018 was relatively low compared to other years. This directly reflects that the uplifts occurring in P2 and P3 in 2018 had a smaller relationship with the precipitation. We speculate that artificial groundwater recharge measures directly increased the groundwater level, enhancing the neutral stress and resulting in significant surface uplift; additionally, the soil and geological structure of the Wuxi area may also have a certain impact on this deformation trend, which will be specifically explained in Section 5.4.

In summary, precipitation affects the surface flotation effect through rainwater infiltration, increasing the soil pore volume and leading to soil layer expansion and surface rebound. However, for certain periods, the impact of precipitation on the surface is not significant, as surface elevation is influenced by a combination of multiple factors. Furthermore, this section also provides an analysis of the correlation coefficients between precipitation and surface changes, which are 0.67 (P1), 0.72 (P2), 0.71 (P3), and 0.70 (P4), confirming that the influence of precipitation is relatively limited.

5.4. The Impact of Soil Stratigraphy and Quaternary Sedimentary Regions

Wuxi, situated in the heart of the Yangtze River Delta, is a vital city linking the Yangtze River and Taihu Lake. The region is characterized by plains interspersed with low mountains and hills [22]. To study the soil layer distribution's impact on surface fluctuation, we obtained data for three typical boreholes in Wuxi from the China Geological Science Institute, focusing on soil layers within 100 m depth: BH_a is near Wanda Plaza in Jiangyin City, close to P3, reaching a final depth of 99.2 m; BH_b is near the intersection of the Shudong River and Outer Ring South Road in Jiangyin City, close to P2, with a final depth of 94.8 m; and BH_c is in the eastern part of the Shuofang Airport area in the Xinwu District of Wuxi City, with a final depth of 92 m. The specific borehole distribution and internal rock and soil distribution are shown in Figure 13.

As shown in Figure 13, Wuxi has a complex stratigraphic structure, with sub-clay, silt, and clay in the upper part, and sub-clay and sub-sandy soil in the lower part, together forming the soft soil layer of Wuxi. During the Quaternary sedimentation process, affected by sea–land alternation, changes in the Yangtze River water level, and river course changes, the region has a complex lithology, characterized by multiple cohesive soil layers and alternating loose sand layers—the direct reason for this sub-clay and silt interlayering is described in [62]. Additionally, Wuxi's stratigraphic changes are highly uneven horizontally. Through geological drilling and controlled-source audio-frequency magnetotellurics, Wu et al. found that the resistivity of the Quaternary loose layer in this region varies greatly horizontally, reflecting differences in the strata's physical properties and directly impacting surface deformation [63].

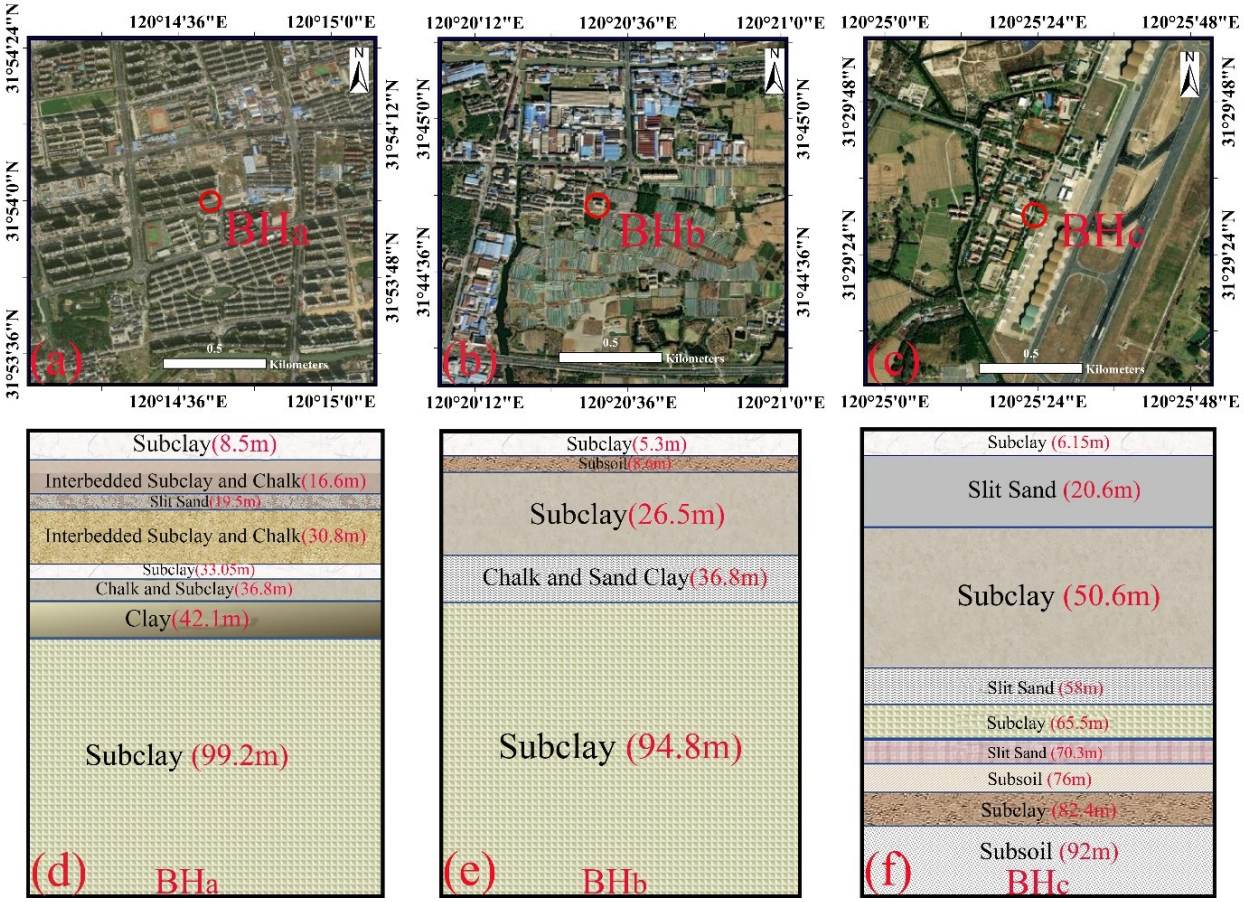

Figure 13. (**a**–**c**) The specific positions of holes BH_a, BH_b, and BH_c, respectively, shown on optical images. (**d**–**f**) Cross-sectional geological maps of the respective points. The red numbers indicate the bottom soil depths and the black text shows the Quaternary geology.

The groundwater level in Wuxi is generally between −1 and −30 m, with the soil mainly consisting of silt and sub-clay in the soft soil layer [64]. The sub-clay has poor permeability and a dense structure, making water flow difficult, while the silt has a looser structure and good permeability. Thus, groundwater mainly affects surface deformation through the silt layer. Early excessive groundwater extraction caused a sharp drop in the water level, leading to severe water loss in some silt layers. Meanwhile, rapid industrial development increased the surface load pressure, compressing the silt layer, reducing pores, and making the structure denser, directly causing large-scale subsidence. In recent years, Wuxi City's groundwater extraction ban has greatly replenished moisture in the silt layer, resulting in elastic surface changes. However, this rebound has limits. Whether in cohesive or sandy soil, long-term compression causes irreversible inelastic deformation, and pore closure makes re-entry difficult. Even with substantial groundwater recharge, the surface is unlikely to return to its original height. As described in the analysis in Section 5.3, P2 and P3 showed significant uplift in 2018 due to groundwater recharge and increased water levels. However, the uplift slowed significantly, even subsiding, after 2019 as the soil layer's inelastic deformation recovered and mostly became plastic. Moreover, the pores could not continue expanding, and water could not re-enter, causing the trend shown in Figure 12.

Overall, the Wuxi area's soil layers primarily comprise sub-sand and silty clay. As these are relatively soft, they strongly correlate with the volatility of the surface deformation in this area. Moreover, overly low groundwater levels can cause inelastic deformation, leading to lasting, irreversible harm; thus, we should strengthen the real-time monitoring of soil layer deformation and groundwater levels.

5.5. Surface Deformation Volatility Evaluation—Amplitude Factor

Continuous land subsidence or uplift decreases the stability of the land. When surface deformation exceeds a certain threshold, it can significantly damage the surrounding buildings and infrastructure. Thus, monitoring and evaluating land surface deformation is crucial. Traditional regional evaluation methods consider factors like crack characteristics, soil/rock properties, and human activities based on study area characteristics [65,66]. However, vast study areas, high difficulty in surveying, and multiple data sources can lead to missing data. Moreover, conventional land surface stability evaluation methods usually assess larger areas but may lack accuracy for specific engineering constructions and earthquake disaster reduction [48]. Therefore, our study designed a new evaluation system based on the GARCH model and proposes a new evaluation indicator—the Amplitude Factor. This method evaluates surface deformation via mathematical simulation, requiring less computational workload and fewer independent variables, suitable for InSAR procedural calculations. In the GARCH model, the important parameter "conditional variance" directly reflects the magnitude of volatility, while the mean, standard deviation, kurtosis, and median reflect the amplitude, stability, kurtosis, and central tendency of data fluctuations, respectively. Per the algorithm in Section 3.3, we obtained the land surface stability evaluation results for Wuxi (Figure 14a).

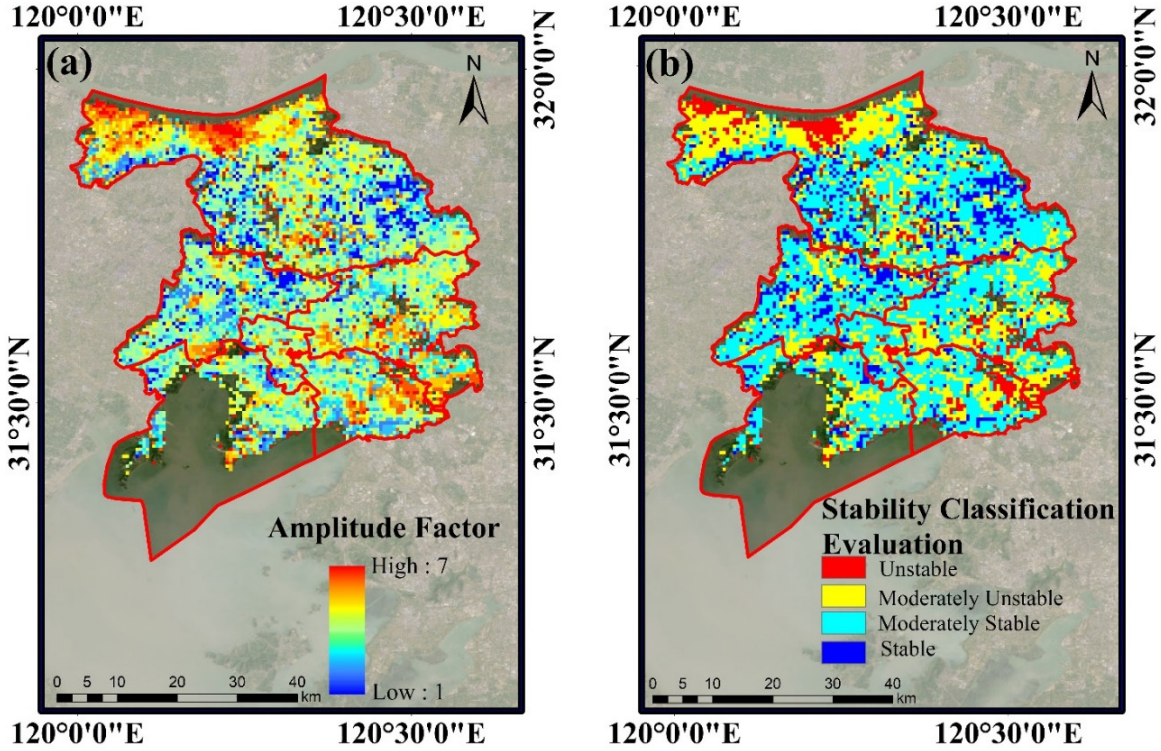

Figure 14. (**a**) Distribution of the Amplitude Factor values in the Wuxi area. (**b**) Classification map of the levels of surface stability in the Wuxi area.

Figure 14a shows that the northern riverside of Jiangyin City has poor stability, with over 64.29% of the Amplitude Factors being over 5.4. Additionally, the southeastern junction of Xishan and Xinwu Districts and the Taihu Lake coastal area of Binhu District exhibit unstable change characteristics. These deformation characteristics align with the velocity field change trend analyzed in Section 4.1, verifying the model's accuracy. Per the scoring system shown in Table 2 of Section 3.3, Wuxi's minimum Amplitude Factor is 1 and its maximum is 7.

To qualitatively assess the volatility of surface deformation, we employed equal interval classification (Figure 14b). Most Wuxi areas are sub-stable or relatively stable,

suggesting that the 2005 groundwater extraction ban yielded notable results. The northern Jiangyin riverside, dominated by alternating silt and clay layers, is highly susceptible to fluctuations in the Yangtze River level, leading to compromised stability. Overall, the Wuxi surface stability evaluation model demonstrates significant precision, offering valuable urban planning and construction guidance. This could ensure urban safety and preserve the success of future major projects in the new era.

5.6. Limitations and Prospects

Our study utilized PS-InSAR monitoring technology to collect land surface deformation data in the Wuxi area from 2015 to 2023. By comparing these with previous studies (see Table 3), we found that the monitoring results are basically consistent. For the first time, we discovered that over a long time period, the land surface in this area did not continuously subside or uplift but showed an alternating trend of changes. However, due to the limited scope of this study, we only conducted a long-term time-series analysis of the trends in the Wuxi area. We suggest that future researchers conduct similar long-term time-series analyses on the Su-Xi-Chang area or even other regions throughout China and the world to verify if this alternating trend exists only in Wuxi, affected by groundwater recharge, or if other non-recharged areas also exhibit this fluctuating trend.

When analyzing and predicting this volatility, we pioneered using the GARCH model from the financial field for fitting and derivation. We designed a land surface volatility indicator—the Amplitude Factor—and conducted a quantitative analysis of unstable changes in the land surface. For the values in Table 2 of Section 3.3, we conducted a comprehensive scoring of land surface deformation characteristics in Wuxi. However, the scoring method used may only be applicable to this area. Whether it is applicable to Su-Xi-Chang or even all of China remains a question worth exploring. Therefore, we recommend that future researchers use this model to analyze different regions to obtain a set of parameters with wider applicability.

According to our research, due to increased attention from modern managers on land surface subsidence and deformation, the deformation of the land surface in Wuxi is no longer like it was in the past (i.e., continuous large-scale subsidence), but instead shows a more fluctuating trend. However, this trend may still pose significant hidden dangers to urban development and infrastructure construction. Therefore, future urban builders should pay more attention to monitoring the volatility of surface deformation and conduct more detailed research and planning on key areas (such as industrial parks, subway lines, and intensively commercial areas), analyzing internal causes according to specific situations and proposing corresponding solutions.

6. Conclusions

This study utilized 100 Sentinel-1A images from November 2015 to June 2023 to investigate the spatiotemporal characteristics of surface deformation in the Wuxi area using the PS-InSAR technique. To better understand the causes of volatility changes, a comprehensive analysis of groundwater, precipitation, soil geology, and other aspects was conducted. Additionally, an Amplitude Factor index was developed to assess the surface stability in the Wuxi area.

The main findings are as follows:

(1) The internal accuracy of PS-InSAR was verified using the precision quality factor evaluation method, revealing that most errors are within 7mm, with almost no errors exceeding 10mm, indicating a high accuracy.

(2) Surface deformation in the Wuxi area is highly uneven, with significant spatial and temporal variations. The northern Jiangyin City area experienced strong surface deformation from 2015 to 2018, which slowed down slightly but showed significant uplift after 2021. The southern Binhu District and Xinwu District experienced substantial subsidence in 2016, followed by minor fluctuations, with the Binhu District experiencing some subsidence again from 2022 to 2023. Over time, the subsidence

amplitude of all PS points has gradually decreased, with more than 90% of the characteristic points having a subsidence rate of 0–4 mm/year after 2018, while the uplift amplitude fluctuates.

(3) Multiple natural factors influence surface volatility in the Wuxi area. This study focused on analyzing the combined effects of groundwater, precipitation, and soil geology. Data from six groundwater-monitoring wells showed a strong correlation between groundwater level changes and surface deformation. For wells (C) and (F), the analysis revealed that surface changes are not only related to precipitation, groundwater abstraction bans, and recharge but also to the area's soft-soil geology. Sandy soil and clay are prone to water loss, shrinkage, and deformation under load pressure, further increasing the surface volatility.

(4) The GARCH model was used to analyze the time-series subsidence displacement in Wuxi City in recent years. By comprehensively analyzing the Conditional Heteroscedasticity model's mean, standard deviation, kurtosis, and median, an innovative "Amplitude Factor" surface volatility evaluation index was developed. The surface stability of the Wuxi area was qualitatively displayed using a hierarchical grading method based on the magnitude of the Amplitude Factor. This analysis found that sub-stable areas are primarily concentrated in northern Jiangyin City and the southeastern junction of Xinwu District and Xishan District, consistent with the research results presented in the previous text.

These findings provide insights into the surface deformation characteristics of Wuxi following groundwater abstraction bans and recharge, offering a basis for future construction and safety control processes undertaken by the local government. Continuous monitoring and analysis of surface volatility changes in the Wuxi area are essential for the city's future safety and development.

Supplementary Materials: The following supporting information can be downloaded at https://www.mdpi.com/article/10.3390/rs16091568/s1, Table S1. Specific parameters of sentinel-1A datasets; Figure S1. Cross-validation results. The deformation magnitude of Dataset I during the period from December 2016 to December 2017 (a). The deformation magnitude of Dataset II during the same period (b). Scatter comparison between Dataset I and II (LOS direction) (c).

Author Contributions: All authors contributed to the manuscript and discussed the results. S.Z. and S.N. put forward the idea of this paper. L.X. processed and analyzed the Sentinel data. S.Z. and R.L. contributed to the manuscript of this paper. S.N. made criticism and revised the manuscript. L.C. and F.S. analyzed the relationship between precipitation, ground water, and ground deformation. S.W. analyzed the results of PS-InSAR. All authors have read and agreed to the published version of the manuscript.

Funding: This work was supported by the National Training Program of Innovation and Entrepreneurship for Undergraduates (grant number S202310359326) and the National Key R&D Program of China (grant number 2021YFB3900604-04/05).

Data Availability Statement: Data incorporated in this research are available for free through the following webpages: Sentinel-1A (https://search.asf.alaska.edu/#/, accessed on 15 September 2023); groundwater level data (http://www.jsgs.com.cn/, accessed on 10 October 2023); weather data (https://data.cma.cn/, accessed on 11 October 2023); 30 m SRTM DEM (https://srtm.csi.cgiar.org/srtmdata/, accessed on 16 October 2023); satellite POD (https://dataspace.copernicus.eu, accessed on 15 October 2023); geological drilling data (http://www.cags.cgs.gov.cn/, accessed on 18 October 2023).

Acknowledgments: We are grateful to the European Space Agency for providing the Sentinel-1Adata and POD data for free. We would also like to thank NASA for providing the SRTM3 DEM data. The authors would like to express our sincere gratitude to the anonymous reviewers for their insightful comments and suggestions.

Conflicts of Interest: The authors declare no conflicts of interest.

References

1. Wu, S.; Yang, Z.; Ding, X.; Zhang, B.; Zhang, L.; Lu, Z. Two Decades of Settlement of Hong Kong International Airport Measured with Multi-Temporal InSAR. *Remote Sens. Environ.* **2020**, *248*, 111976. [CrossRef]
2. He, Y.; Ng, A.H.-M.; Wang, H.; Kuang, J. Understanding the Spatiotemporal Characteristics of Land Subsidence and Rebound in the Lianjiang Plain Using Time-Series InSAR with Dual-Track Sentinel-1 Data. *Remote Sens.* **2023**, *15*, 3236. [CrossRef]
3. Wang, Y.; Chen, X.; Wang, Z.; Gao, M.; Wang, L. Integrating SBAS-InSAR and Random Forest for Identifying and Controlling Land Subsidence and Uplift in a Multi-Layered Porous System of North China Plain. *Remote Sens.* **2024**, *16*, 830. [CrossRef]
4. Chen, Y.; Ding, C.; Huang, P.; Yin, B.; Tan, W.; Qi, Y.; Xu, W.; Du, S. Research on Time Series Monitoring of Surface Deformation in Tongliao Urban Area Based on SBAS-PS-DS-InSAR. *Sensors* **2024**, *24*, 1169. [CrossRef] [PubMed]
5. Zhang, Y.; Wu, J.; Xue, Y.; Wang, Z.; Yao, Y.; Yan, X.; Wang, H. Land Subsidence and Uplift Due to Long-Term Groundwater Extraction and Artificial Recharge in Shanghai, China. *Hydrogeol. J.* **2015**, *23*, 1851–1866. [CrossRef]
6. Novellino, A.; Pennington, C.; Leeming, K.; Taylor, S.; Alvarez, I.G.; McAllister, E.; Arnhardt, C.; Winson, A. Mapping landslides from space: A review. *Landslides* **2024**, *21*, 1041–1052. [CrossRef]
7. Wyss, M.; Speiser, M.; Tolis, S. Earthquake Fatalities and Potency. *Nat. Hazards* **2023**, *119*, 1091–1106. [CrossRef]
8. Sim, K.B.; Lee, M.L.; Wong, S.Y. A Review of Landslide Acceptable Risk and Tolerable Risk. *Geoenviron. Disasters* **2022**, *9*, 3. [CrossRef]
9. Shi, W.; Chen, G.; Meng, X.; Jiang, W.; Chong, Y.; Zhang, Y.; Dong, Y.; Zhang, M. Spatial-Temporal Evolution of Land Subsidence and Rebound over Xi'an in Western China Revealed by SBAS-InSAR Analysis. *Remote Sens.* **2020**, *12*, 3756. [CrossRef]
10. Nikos, S.; Ioannis, P.; Constantinos, L.; Paraskevas, T.; Anastasia, K.; Charalambos (Haris), K. Land Subsidence Rebound Detected via Multi-Temporal InSAR and Ground Truth Data in Kalochori and Sindos Regions, Northern Greece. *Eng. Geol.* **2016**, *209*, 175–186. [CrossRef]
11. Gerardo, H.; Pablo, E.; Roberto, T.; Marta, B.; Juan, L.; Mauro, R.; Maria, M.; Dora, C.; John, L.; Pietro, T. Mapping the global threat of land subsidence. *Science* **2021**, *371*, 34–36. [CrossRef] [PubMed]
12. Poland, M.; Bürgmann, R.; Dzurisin, D.; Lisowski, M.; Marsterlark, T.; Owen, S.; Fink, J. Constraints onthe mechanism of long-term, steady subsidence at Medicine Lake volcano, northern California, from GPS, leveling, and InSAR. *J. Volcanol. Geotherm. Res.* **2006**, *150*, 55–78. [CrossRef]
13. Guo, J.; Zhou, L.; Yao, C.; Hu, J. Surface Subsidence Analysis by Multi-Temporal InSAR and GRACE: A Case Study in Beijing. *Sensors* **2016**, *16*, 1495. [CrossRef] [PubMed]
14. Furst, S.L.; Doucet, S.; Vernant, P.; Champollion, C.; Carme, J.-L. Monitoring surface deformation of deep salt mining in Vauvert (France), combining InSAR and leveling data for multi-source inversion. *Solid Earth* **2021**, *12*, 15–34. [CrossRef]
15. Huang, B.; Zheng, F.; Bai, J.; Wang, Y. Feasibility of land surface deformation monitoring by regional CORS. *J. Geomat. Sci. Technol.* **2011**, *28*, 169–172.
16. Chen, Q.; Liu, G.; Hu, Z.; Ding, X.; Yang, Y. Mapping ground 3-D displacement with GPS and PS-InSAR networking in the Pingtung area, southwestern Taiwan. *Chin. J. Geophys.* **2012**, *55*, 3248–3258.
17. Dong, J.; Zhang, L.; Tang, M.; Liao, M.; Xu, Q.; Gong, J.; Ao, M. Mapping Landslide Surface Displacements with Time Series SAR Interferometry by Combining Persistent and Distributed Scatterers: A Case Study of Jiaju Landslide in Danba, China. *Remote Sens. Environ.* **2018**, *205*, 180–198. [CrossRef]
18. He, P. Error Analysis and Surface Deformation Application of Time Series InSAR. Ph.D. Thesis, Wuhan University, Wuhan, China, March 2014.
19. Zhang, T. Advanced Coregistration Methods of Sentinel-1 A/B Satelliates and Its Application in Tianjin Area. Ph.D. Thesis, Wuhan University, Wuhan, China, May 2019.
20. Zhao, Y.; Zhou, L.; Wang, C.; Li, J.; Qin, J.; Sheng, H.; Huang, L.; Li, X. Analysis of the Spatial and Temporal Evolution of Land Subsidence in Wuhan, China from 2017 to 2021. *Remote Sens.* **2022**, *14*, 3142. [CrossRef]
21. Sajjad, M.M.; Wang, J.; Afzal, Z.; Hussain, S.; Siddique, A.; Khan, R.; Ali, M.; Iqbal, J. Assessing the Impacts of Groundwater Depletion and Aquifer Degradation on Land Subsidence in Lahore, Pakistan: A PS-InSAR Approach for Sustainable Urban Development. *Remote Sens.* **2023**, *15*, 5418. [CrossRef]
22. Wuxi Natural Resources and Planning Bureau. Available online: https://zrzy.wuxi.gov.cn/doc/2017/06/09/1645686.shtml (accessed on 9 December 2023).
23. Hu, J. A Study on the Land Subsidence Effect after Prohibiting Extraction of Groundwater in Suzhou-Wuxi-Changzhou Area. Ph.D. Thesis, Nanjing University, Nanjing, China, January 2011.
24. Karanasos, M. The Second Moment and the Autocovariance Function of the Squared Errors of the GARCH Model. *J. Econom.* **1999**, *90*, 63–76. [CrossRef]
25. Huang, H.; Leng, X.; Liu, X.; Peng, L. Unified Inference for an AR Process Regardless of Finite or Infinite Variance GARCH Errors. *J. Financ. Econom.* **2019**, *18*, 425–470. [CrossRef]
26. Nazeri-Tahroudi, M.; Ramezani, Y.; De Michele, C.; Mirabbasi, R. Bivariate Simulation of Potential Evapotranspiration Using Copula-GARCH Model. *Water Resour. Manag.* **2022**, *36*, 1007–1024. [CrossRef]
27. Engle, R. GARCH 101: The Use of ARCH/GARCH Models in Applied Econometrics. *J. Econ. Perspect.* **2001**, *15*, 157–168. [CrossRef]

28. Aloui, R.; Ben Aïssa, M.S. Relationship between Oil, Stock Prices and Exchange Rates: A Vine Copula Based GARCH Method. *N. Am. J. Econ. Financ.* **2016**, *37*, 458–471. [CrossRef]
29. Lu, Y. Land Subsidence Monitoring and Analysis of Influencing Factors in Su-Xi-Chang Area Based on Multi-Source SAR Data. Ph.D. Thesis, Nanjing University, Nanjing, China, May 2018.
30. Yu, J.; Li, Z.; Wu, J. Research on the Application of InSAR/GPS Integrated Technology in Ground Subsidence Monitoring in Changzhou-Wuxi. *Prog. Nat. Sci.* **2009**, *19*, 1267–1271.
31. Ouyang, S.; Zhou, S.; Zhou, Z. Surface deformation monitoring in the downtown of Wuxi with PS-InSAR technology. *Beijing Surv. Mapp.* **2022**, *36*, 194–199.
32. Wuxi Meteorological Bureau, Jiangsu Province. Available online: http://js.cma.gov.cn/dsjwz/wxs/njszfxxgk/sjfdzdgknr/sjtjxx/202203/t20220307_4565613.html (accessed on 10 October 2023).
33. Yang, C.; Lv, S.; Hou, Z.; Zhang, Q.; Li, T.; Zhao, C. Monitoring of Land Subsidence and Ground Fissure Activity within the Su-Xi-Chang Area Based on Time-Series InSAR. *Remote Sens.* **2022**, *14*, 903. [CrossRef]
34. Ferretti, A.; Prati, C.; Rocca, F. Permanent scatterers in SAR interferometry. *IEEE Trans. Geosci. Remote Sens.* **2001**, *39*, 8–20. [CrossRef]
35. Raucoules, D.; Le Mouelic, S.; Carnec, C.; Maisons, C.; King, C. Urban subsidence in the city of Prato (Italy) monitored by satellite radar interferometry. *Int. J. Remote Sens.* **2003**, *24*, 891–897. [CrossRef]
36. Babu, A.; Kumar, S. PSInSAR Processing for Volcanic Ground Deformation Monitoring Over Fogo Island. *Proceedings* **2019**, *24*, 3. [CrossRef]
37. Khorrami, M.; Abrishami, S.; Maghsoudi, Y.; Alizadeh, B.; Perissin, D. Extreme Subsidence in a Populated City (Mashhad) Detected by PSInSAR Considering Groundwater Withdrawal and Geotechnical Properties. *Sci. Rep.* **2020**, *10*, 11357. [CrossRef] [PubMed]
38. Li, J.; Zhou, L.; Ren, C.; Liu, L.; Zhang, D.; Ma, J.; Shi, Y. Spatiotemporal Inversion and Mechanism Analysis of Surface Subsidence in Shanghai Area Based on Time-Series InSAR. *Appl. Sci.* **2021**, *11*, 7460. [CrossRef]
39. Zhou, L.; Liu, S.; Li, J.; Pan, Y.; Wang, C.; Huang, L.; Huang, L. Investigating surface deformation and its intrinsic mechanism in Shenzhen, China using Sentinel-1A SAR imagery. *Earth Space Sci.* **2023**, *10*, e2023EA002905. [CrossRef]
40. Hooper, A. A Multi-Temporal InSAR Method Incorporating Both Persistent Scatterer and Small Baseline Approaches. *Geophys. Res. Lett.* **2008**, *35*, L16302. [CrossRef]
41. Jiang, S. Application of PSInSAR Technology in Monitoring Highway Subsidence. Ph.D. Thesis, East China Jiaotong University, Nanchang, China, June 2018.
42. Zhou, L. Monitoring and Analysis of Surface Subsidence and Building Deformation by Radar Interferometry. Ph.D. Thesis, Wuhan University, Wuhan, China, June 2018.
43. Awasthi, S.; Jain, K.; Bhattacharjee, S.; Gupta, V.; Varade, D.; Singh, H.; Narayan, A.B.; Budillon, A. Analyzing Urbanization Induced Groundwater Stress and Land Deformation Using Time-Series Sentinel-1 Datasets Applying PSInSAR Approach. *Sci. Total Environ.* **2022**, *844*, 157103. [CrossRef] [PubMed]
44. Modarres, R.; Ouarda, T.B.M.J. Modelling Heteroscedasticty of Streamflow Times Series. *Hydrol. Sci. J.* **2013**, *58*, 54–64. [CrossRef]
45. Wang, S.; Li, G.; Wang, J. Volatility Prediction Evaluation of GARCH Models Based on Loss Functions. *Oper. Res. Manag. Sci.* **2023**, *32*, 101–106.
46. Bollerslev, T. The Story of GARCH: A Personal Odyssey. *J. Econom.* **2023**, *234*, 96–100. [CrossRef]
47. Wang, L. Evaluation Method of Financial Volatility Model and Bayesian Volatility Modeling and Application in Empirical Research. Master's Thesis, Nanjing University of Finance and Economics, Nanjing, China, May 2021.
48. The Standing Committee of Jiangsu Provincial People's Congress. Available online: https://www.jsrd.gov.cn/qwfb/sjfg/202110/t20211008_532359.shtml# (accessed on 10 October 2023).
49. Wuxi Natural Resources and Planning Bureau. Available online: https://zrzy.wuxi.gov.cn/doc/2017/10/20/1552374.shtml (accessed on 12 November 2023).
50. Jiangsu Provincial People's Government. Available online: http://www.jiangsu.gov.cn/art/2012/2/15/art_46143_2544341.html (accessed on 12 November 2023).
51. Li, X.; Wang, Y.; Zhao, L.; Ma, Z. Surface subsidence monitoring of Suzhou Wuxi Changzhou urban agglomeration. *Hydrogr. Surv. Charting* **2021**, *41*, 49–53.
52. Fan, X.; Li, M.; Zhang, D.; Zhao, C. Monitoring of Surface Subsidence in Wuxi City with MCTSB-InSAR Method. *Mod. Surv. Mapp.* **2018**, *41*, 1–5.
53. Ouyang, S. Application and Risk Assessment of Urban Surface Deformation Monitoring Based on Time Series InSAR Technology. Master's Thesis, East China University of Technology, Nanchang, China, June 2022.
54. Tang, W.; Zhao, X.; Motagh, M.; Bi, G.; Li, J.; Chen, M.; Chen, H.; Liao, M. Land Subsidence and Rebound in the Taiyuan Basin, Northern China, in the Context of Inter-Basin Water Transfer and Groundwater Management. *Remote Sens. Environ.* **2022**, *269*, 112792. [CrossRef]
55. Wuxi Liangxi District People's Government. Available online: https://www.wxlx.gov.cn/doc/2021/07/09/3353129.shtml (accessed on 25 November 2023).
56. Xia, J. *Soil Mechanics and Engineering Geology*, 1st ed.; Zhejiang University Press: Nanjing, China, 2012; pp. 148–149.

57. Cao, Y.; Wei, Y.; Fan, W.; Peng, M.; Bao, L. Experimental Study of Land Subsidence in Response to Groundwater Withdrawal and Recharge in Changping District of Beijing. *PLoS ONE* **2020**, *15*, e0232828. [CrossRef] [PubMed]
58. Zhao, J. Application of InSAR Technology in Surface Deformation Monitoring. Master's Thesis, Nanjing University, Nanjing, China, May 2019.
59. Shen, C. Analysis of detrended time-lagged cross-correlation between two nonstationary time series. *Phys. Lett. A* **2015**, *379*, 680–687. [CrossRef]
60. The Central People's Government of the People's Republic of China. Available online: https://www.gov.cn/zhengce/zhengceku/2021-04/26/content_5602408.htm (accessed on 29 November 2023).
61. Ye, H.; Tang, X.; Hu, J.; Wu, C.; Su, L.; Chen, J.; Huang, L. Soil Infiltration Coefficient and Influencing Factors in Nanping City Under the Background of Sponge City Construction. *J. Yichun Univ.* **2023**, *45*, 85–90.
62. Tang, J. Geological conditions and evaluation of shallow foundation engineering in Wuxi urban area. *J. Shuzhou Railw. Teach. Coll.* **1994**, *11*, 52–55.
63. Wu, J.; Zhou, G.; Wu, S.; Li, W.; Ming, W. Research on earth fissures in Guangming Village of Wuxi City. *J. Geol.* **2013**, *37*, 203–207.
64. Wang, G.; Zhu, J.; Zhang, D.; Wu, J.; Yu, J.; Gong, X.; Gou, F. Land Subsidence and Uplift Related to Groundwater Extraction in Wuxi, China. *Q. J. Eng. Geol. Hydrogeol.* **2020**, *53*, 609–619. [CrossRef]
65. Shuren, W.; Danggong, H.; Qingxuan, C.; Ruichun, X.; Yingtang, M. Assessment of the Crustal Stability in the Qingjiang River Basin of the Western Hubei Province and Its Peripheral Area, China. In *Engineering Geology*; CRC Press: Boca Raton, FL, USA, 2021; pp. 375–385. [CrossRef]
66. Xiao, W.; Zhang, J.; Zhu, J.; Zhang, Z.; Cai, H.; Zhang, P.; Jia, R. Evaluation of crustal stability in southern Taiyuan based on GIS platform. *Miner. Explor.* **2021**, *12*, 1655–1661.

Disclaimer/Publisher's Note: The statements, opinions and data contained in all publications are solely those of the individual author(s) and contributor(s) and not of MDPI and/or the editor(s). MDPI and/or the editor(s) disclaim responsibility for any injury to people or property resulting from any ideas, methods, instructions or products referred to in the content.